Research Square

Preprints are preliminary reports that have not undergone peer review.
They should not be considered conclusive, used to inform clinical practice,
or referenced by the media as validated information.

DJAMILAR: Reconstructing the Geometry of the Quantum–Classical Transition — A Common-Aperture Test Linking Matter-Wave Coherence and Mechanical Fluctuations

ANISSE ZEROUTA

a.zerouta@precogtec.com

Precog Technologies– Theoretical Physics Division https://orcid.org/0000-0001-7966-0746

Research Article

Keywords: quantum–classical transition, geometric localization, matter-wave interference, non-Gaussian fluctuations, inverse problems, DJAMILAR

Posted Date: September 29th, 2026

DOI: https://doi.org/10.21203/rs.3.rs-11189947/v1

License: This work is licensed under a Creative Commons Attribution 4.0 International License.
Read Full License

Additional Declarations: The authors declare no competing interests.

DJAMILAR: Reconstructing the Geometry of the Quantum–Classical Transition

A common-aperture test linking matter-wave coherence and mechanical fluctuations

Anisse Zerouta

Theoretical Physics Division, Precog Technologies
Paris, France
a.zerouta@precogtec.com

25 September 2026

Abstract

DJAMILAR proposes that a common geometric aperture controls collective localization, spatial resolution and the associated momentum transfers. We turn this identification into an inverse problem with independent experimental consequences. For the finite-rate Gaussian localization channel, second and fourth mechanical cumulants determine the aperture and event rate, which then predict interference attenuation without localization refitting. Higher cumulants test the transfer kernel. We prove that the single-aperture prediction minimizes decoherence at fixed second and fourth cumulants within positive mixtures of Gaussian transfer channels. The same diagnostics test standard Gaussian-smearing CSL for an extended homogeneous sphere: its dimensionless cumulant ratio falls below the mixture bound near the size crossover and tends to 15/7, rather than unity, for large spheres. An exact free-flight likelihood gives a quantitative reconstruction window. With known Gaussian background variance equal to the channel contribution, 30 000 synthetic mechanical trials yield 3.2% aperture precision and a successful independent coherence prediction. A fixed-apparatus Fisher map quantifies the loss of precision at lower normalization. The preparation budget also exposes a mass cancellation: for linear amplification, the channel variance divided by the minimum spread of an uncorrelated pure Gaussian preparation is independent of mass except through geometric activation. A separate size scan completes the common-aperture test. The inverse method extends to other Gaussian localization generators; the additional DJAMILAR commitment is agreement with an independently inferred activation length and a specified geometric state. Numerical reconstructions are synthetic, and the sensitivity map assumes exactly known background. Experimental implementation, signal attribution and gravitational state transfer remain distinct physical tasks.

Keywords: quantum–classical transition; geometric localization; matter-wave interference; non-Gaussian fluctuations; inverse problems; DJAMILAR.

1 From a geometric hypothesis to an independently testable length

The central physical proposition of DJAMILAR is that a microscopic geometric structure can govern phenomena usually treated separately: gravitational response, the loss of spatial coherence and the emergence of approximately classical motion. Its proposed apertures, the Djamilars, are represented collectively by a geometric loading and an effective state. The founding filtration proposal introduced this physical picture [1]; the gravitational representative supplied dynamical equations and matching requirements [2]; the quantum companion formulated a completely positive localization channel and its collective activation law [3]. A natural next question is whether the aperture can be reconstructed from observations that constrain different aspects of the mechanism.

This paper develops that question into a test. A size scan determines how localization activates. An interference scan determines how the channel resolves spatial alternatives. A mechanical distribution determines the scale of its momentum transfers. If the proposed identification is correct, these three procedures recover a common length,

$$r_A = r_I = r_M = r_d. \tag{1}$$

The subscripts denote activation, interference and mechanics. They label independent estimands before the equality is tested. In particular, fitting all observations with a radius constrained to be common establishes a joint fit, but does not by itself test the equality in Eq. (1).

The mechanical route requires more information than a force-noise spectrum. A spectrum measures a second moment. Different event rates and transfer amplitudes can produce that same moment. The finite-event channel retains a further signature in its fourth and higher cumulants. Resolving that signature separates the rate from the aperture, and permits an interference prediction made from mechanical data alone. The physical claim can therefore be stated directly: *the geometry inferred from the shape of mechanical fluctuations must predict how quantum coherence disappears.*

The relation between momentum-transfer statistics and decoherence belongs to the established theory of translation-covariant open dynamics [4, 5, 6]. Gaussian localization also has a long history in dynamical reduction [7, 8]. Inferring the rate and jump law of a compound Poisson process is an established inverse problem, known as decompounding [9]. Higher-order noise spectroscopy likewise reconstructs information beyond a power spectrum and connects it to quantum-probe dynamics [10, 11]. We use these structures explicitly. The contribution developed here is their operational inversion in the DJAMILAR programme, the independent prediction and common-aperture comparison, a bound for heterogeneous Gaussian channels, and a preparation-sensitive experimental design calculation. Neither a Poisson representation nor a nonzero fourth cumulant is, by itself, evidence for a geometric microscopic origin.

The two experimental traditions joined by this construction are already well developed separately. Matter-wave experiments have quantitatively resolved collisional and thermal-radiation decoherence [12, 13], and coherent propagation has progressed from complex molecules beyond 25 kDa [14] to sodium nanoparticles above 170 kDa [15]. Complementary non-interferometric searches use precision mechanical noise to constrain stochastic localization, including ultracold cantilevers and engineered force sensors [16, 17, 18]. The distinctive proposition tested here is a common-aperture cross-prediction: higher mechanical cumulants fix the localization width and rate, those parameters are transported without localization refitting into an independent coherence measurement, and a separately inferred activation radius then tests whether the same length has a geometric interpretation.

The inverse is also applicable to GRW-type rigid-body centre-of-mass dynamics and to the point-body limit $R \ll r_C$ of standard mass-proportional continuous spontaneous localization (CSL), when their reduced generator has the same Gaussian transfer form [7, 8, 19]. The effective rate and its amplification remain model dependent. Equality of reduced generators does not identify their stochastic unravelings. Extended-body CSL retains its mass-density form factor; Section 7.3 calculates the resulting departure from a single inferred width. Occupancy of order unity can preserve non-Gaussian information, but resolving that information still requires an adequate preparation and measurement budget.

The qubit protocols in Refs. [10, 11] establish relevant methods for characterizing non-Gaussian dephasing; they do not demonstrate the nanoparticle mechanics–interference experiment proposed here. In the present construction, the additional physical commitment is that the mechanically inferred transfer width must also agree with the independently inferred size-activation length.

There are three levels of physical interpretation. Agreement between mechanics and interference supports a shared localization generator. Agreement with the independently inferred

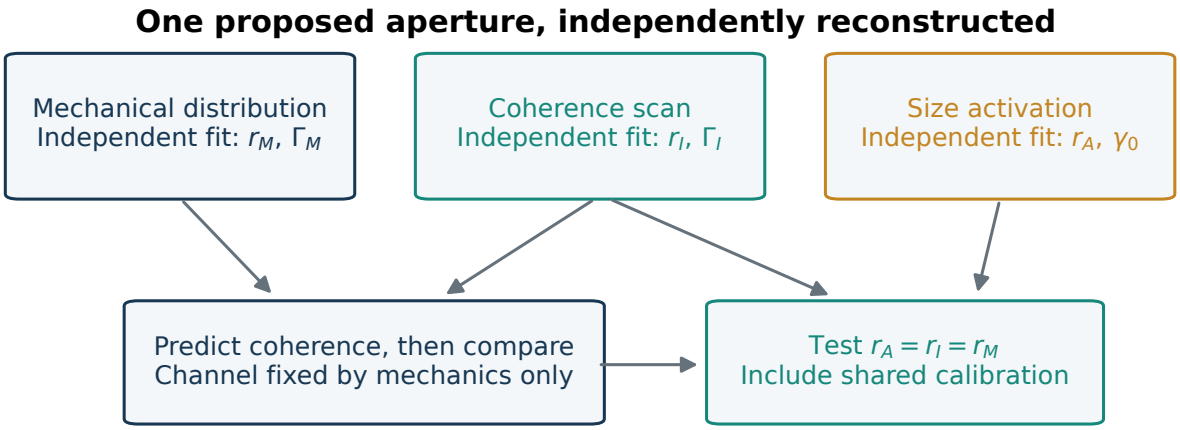


Figure 1: Operational structure of the common-aperture test. Mechanical data first fix a channel and its uncertainty, from which an interference signal is predicted. Separate fits to interference and size activation give the remaining length reconstructions. Their equality is a subsequent test. All routes require their own conventional-background and apparatus models.

activation radius supports the additional geometric identification in Eq. (1). Connecting its variation to a gravitational state calculated from source and boundary data would test the wider programme. These levels remain distinguishable throughout the analysis.

2 One aperture, three observable responses

2.1 Material domain and geometric state

We consider a fixed, maximal bound rigid domain of mass M and physical radius R. The material radius is distinct from a path separation d and from the aperture r_d. The domain must remain the same physical object across the measurements being compared. In the rigid-domain regime, internal relative displacements satisfy $\sigma_{\mathrm{rel}} \ll r_d$; fragmentation, rearrangement or a change in the assumed collective domain is a change of model, not a free normalization adjustment [3]. Nonspherical domains require a size convention and shape prescription fixed before inference.

The common-state identification in the gravitational representative is

$$C_d = \pi n_d r_d^2, \qquad \vartheta = \ln(C_d/C_{d,\mathrm{ref}}), \tag{2}$$

where n_d is a proper surface density on the specified microscopic cross-section [2]. Thus C_d and ϑ are dimensionless. This paper studies a homogeneous, stationary local state over each run. The aperture is an effective length at that state; its microscopic interpretation is a hypothesis to be constrained.

For inference we initially allow distinct activation and resolving lengths:

$$\Gamma_D(M,R) = \gamma_0 \left(\frac{M}{m_0}\right)^{\alpha} F_p(R/r_A), \qquad F_p(z) = \frac{z^p}{1+z^p}, \tag{3}$$

$$\mathcal{R}(d) = \Gamma_D \left[1 - \exp\left(-\frac{d^2}{4r_I^2}\right)\right]. \tag{4}$$

Here m_0 is the atomic mass unit, γ_0 has units of inverse time and $p > 0$. The reference realization uses $\alpha = 1$ and $p = 4$. These values are fixed in the numerical example, not inferred from it. The common-aperture realization sets $r_A = r_I = r_d$ as a physical prediction.

2.2 The exact finite-transfer channel

For a homogeneous aperture, the quantum companion uses

$$\mathcal{L}_D\rho = \Gamma_D \int_{\mathbb{R}^3} \mathrm{d}^3q\, \mu_{r_d}(\mathbf{q}) \left(\mathrm{e}^{i\mathbf{q}\cdot\mathbf{X}/\hbar}\rho \mathrm{e}^{-i\mathbf{q}\cdot\mathbf{X}/\hbar} - \rho \right), \tag{5}$$

$$\mu_{r_d}(\mathbf{q}) = \frac{r_d^3}{\pi^{3/2}\hbar^3} \exp\left(-\frac{r_d^2\mathbf{q}^2}{\hbar^2} \right). \tag{6}$$

The kernel is normalized and isotropic. Along any one axis its transfer variance is

$$\sigma_q^2 = \frac{\hbar^2}{2r_d^2}. \tag{7}$$

The generator produces Eq. (4) with $r_I = r_d$, momentum-variance growth $\Gamma_D\sigma_q^2$ per axis, and three-dimensional kinetic-energy growth $3\Gamma_D\sigma_q^2/(2M)$. Those second-moment relations were established in the earlier articles [2, 3]. Our inverse problem keeps the full transfer process before a diffusion approximation removes its higher cumulants.

The assumptions needed for the derivations are finite positive rate, independent increments, Gaussian isotropic transfer, a stationary local state and known free or linear mechanical propagation. The measured preparation and readout need not be perfect; they must enter the forward model. For nonlinear traps, unresolved state drift or correlated force events, the formulas below are not automatically valid.

Equation (5) admits a compound-Poisson representation. This is a statement about the reduced dynamics and the distributions it predicts. Distinct stochastic unravelings can describe the same reduced evolution. Reconstructing its Poisson parameters does not establish that individual microscopic Djamilars have been counted or that a unique state-reduction ontology has been selected.

3 The geometry encoded in mechanical fluctuations

3.1 Separating rate and aperture

During free evolution, let ΔP denote the momentum added by the channel along one axis in time T. Its characteristic function is

$$\ln \Phi_{\Delta P}(s,T) = \Gamma_D T \left[\exp(-\sigma_q^2 s^2/2) - 1 \right], \qquad [s] = [P]^{-1}. \tag{8}$$

Differentiating at $s = 0$ gives cumulant production rates

$$c_{2n} \equiv \frac{\kappa_{2n}^{(D)}(T)}{T} = (2n-1)!!\,\Gamma_D\sigma_q^{2n}, \qquad c_{2n+1} = 0. \tag{9}$$

These are cumulants added by the channel, not raw moments of an arbitrary measured distribution. Independent contributions add at the cumulant level. The initial distribution, Gaussian readout variance and identifiable environmental channels must be propagated or removed with their uncertainties.

Proposition 1 (Mechanical identification)**.** *For the homogeneous channel in Eqs.* (5)–(6)*, positive resolved values of* c_2 *and* c_4 *uniquely determine*

$$\boxed{r_M^2 = \frac{3\hbar^2 c_2}{2c_4}, \qquad \Gamma_M = \frac{3c_2^2}{c_4}.} \tag{10}$$

Indeed, $c_4/c_2 = 3\sigma_q^2$ fixes the transfer scale, after which c_2/σ_q^2 fixes the rate. The dimensions are explicit: $[c_2/c_4] = [P]^{-2}$, so $\hbar^2 c_2/c_4$ is a squared length, while $[c_2^2/c_4] = \mathrm{s}^{-1}$. The inverse is poorly conditioned when the fourth cumulant is unresolved. A noisy estimate that fluctuates below zero is not evidence for an imaginary radius; it requires likelihood-based inference or an appropriate confidence region at the boundary.

The channel has excess momentum kurtosis

$$g_{2,P}^{(D)} = \frac{\kappa_4^{(D)}}{(\kappa_2^{(D)})^2} = \frac{3}{\lambda}, \qquad \lambda = \Gamma_D T. \tag{11}$$

Small event occupancy preserves a pronounced non-Gaussian distribution. Large occupancy approaches diffusion. This information is absent from a power spectrum even if that spectrum is measured precisely.

3.2 Overdetermining the transfer kernel

The same model fixes the hierarchy

$$\frac{c_6 c_2}{c_4^2} = \frac{5}{3}, \qquad \frac{c_8 c_4}{c_6^2} = \frac{7}{5}. \tag{12}$$

These identities test transfer shape rather than simply estimating a second free parameter. They can fail through non-Gaussian kicks, aperture heterogeneity, nonstationarity or an incorrectly isolated background. The odd cumulants give additional checks for a residual directional force or asymmetric contamination. A resolved fourth cumulant does not guarantee that the sixth and eighth cumulants can be tested at the same sample count. Their uncertainties and sensitivity to rare events must be assessed separately before claiming a measured kernel hierarchy.

An independent additive Gaussian contribution has no cumulants above order two. If it obscures c_2 but leaves sufficiently well-measured fourth and sixth cumulants, an alternative reconstruction is

$$r_{M,46}^2 = \frac{5\hbar^2 c_4}{2c_6}, \qquad \Gamma_{M,46} = \frac{25c_4^3}{3c_6^2}, \qquad c_2^{(D)} = \frac{5c_4^2}{3c_6}. \tag{13}$$

This route is Gaussian-background invariant in the ideal population equations. Its statistical cost is higher: estimating c_6 requires control of tails through order twelve for an asymptotic variance. It does not remove non-Gaussian environmental events or uncertain detector nonlinearities. We consequently use the full convolved distribution for the primary numerical reconstruction.

3.3 What a position detector measures

An event at time s in free flight changes the final position by $q(T-s)/M$. The added position cumulants are therefore

$$\kappa_{2n}^{X,D} = \frac{\Gamma_D (2n-1)!! \sigma_q^{2n} T^{2n+1}}{(2n+1) M^{2n}}. \tag{14}$$

The corresponding inverse is

$$\boxed{\Gamma_D = \frac{27(\kappa_2^{X,D})^2}{5T\kappa_4^{X,D}}, \qquad r_d^2 = \frac{9\hbar^2 T^2}{10M^2}\frac{\kappa_2^{X,D}}{\kappa_4^{X,D}}.} \tag{15}$$

The position excess kurtosis is $27/(5\lambda)$. Applying Eq. (10) directly to position cumulants would give an incorrect radius and rate. More generally, for a calibrated linear impulse response $h_T(s)$,

$$\kappa_n^{Y,D} = \Gamma_D \langle q^n \rangle \int_0^T h_T(s)^n \mathrm{d}s. \tag{16}$$

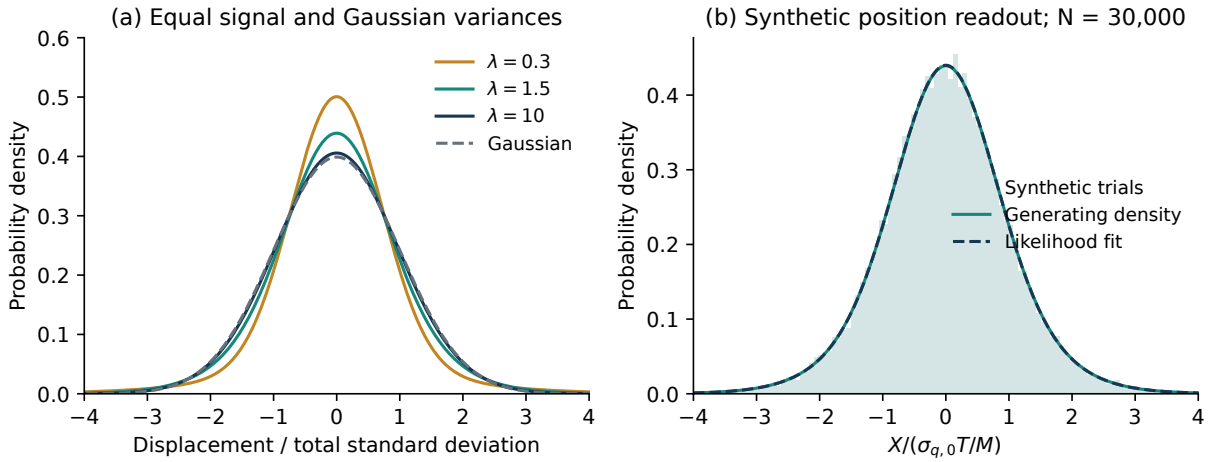


Figure 2: Exact free-flight position distributions after Gaussian preparation and readout convolution. (a) The Gaussian background variance equals the channel variance in each curve, and displacement is standardized by the total standard deviation. Finite occupancy retains a central peak and non-Gaussian tails despite equal total variance after standardization. (b) The reference synthetic sample of 30 000 trials and its likelihood fit. This is a simulated position measurement, not measured nanoparticle data.

Thus the response must be evaluated separately for each cumulant order, as expected in the higher-order correlation and polyspectral description of fluctuations [20]. Appendix B treats the initial quantum state and finite readout duration.

4 Predicting quantum coherence from mechanical measurements

4.1 A prediction with the localization parameters already fixed

Substituting the mechanically reconstructed aperture and rate into the decoherence kernel gives

$$\mathcal{R}_{\mathrm{pred}}(d) = \frac{3c_2^2}{c_4}\left[1 - \exp\left(-\frac{c_4 d^2}{6\hbar^2 c_2}\right)\right]. \tag{17}$$

Mechanical fluctuations determine a spatial decoherence law. No localization parameter is subsequently fitted to the interference observations used to test this prediction.

For a prescribed pair of paths with separation $\Delta\mathbf{x}(t)$, the channel contribution to the attenuation exponent is

$$\mathcal{D}_{\mathrm{pred}}[\Delta\mathbf{x}] = \frac{3c_2^2}{c_4}\int_0^{T_I}\left[1 - \exp\left(-\frac{c_4|\Delta\mathbf{x}(t)|^2}{6\hbar^2 c_2}\right)\right]\mathrm{d}t. \tag{18}$$

Here T_I is the interferometer exposure and need not equal the mechanical calibration duration. Stationarity and a fixed material domain are required for that transfer. If another mass or size is used, the corresponding transfer through Eq. (3) is an additional tested assumption.

The c_4, c_6 reconstruction gives an alternative prediction,

$$\mathcal{R}^{(4,6)}_{\mathrm{pred}}(d) = \frac{25c_4^3}{3c_6^2}\left[1 - \exp\left(-\frac{c_6 d^2}{10\hbar^2 c_4}\right)\right]. \tag{19}$$

Their agreement is a kernel consistency check. The predicted visibility still requires the ordinary visibility V_0, the separation history, detector response and sample distributions. "Without refitting" concerns the localization channel; it does not eliminate these physical inputs.

At small separation,

$$\mathcal{R}(d) = \frac{c_2 d^2}{2\hbar^2} - \frac{c_4 d^4}{24\hbar^4} + \frac{c_6 d^6}{720\hbar^6} + O(d^8). \tag{20}$$

The leading coherence–noise relation was already derived in the companion article [3]. Measuring only this term cannot separate rate and length. The present reconstruction predicts the full resolving curve, including its saturation at Γ_D. In the diffusion limit $\sigma_q^2 \to 0$, $\Gamma_D \to \infty$ at fixed c_2, the fourth cumulant vanishes and only the quadratic law survives. Finite-aperture identification is then lost even though diffusion remains measurable.

4.2 A single aperture is an extremal channel

A failure of the single-Gaussian kernel does not immediately specify its replacement. One controlled extension is a positive superposition of independent Gaussian transfer channels with different variances $u = \sigma_q^2$. Let $\nu(\mathrm{d}u)$ be their rate measure, with the required moments finite, and define

$$A_j = \int_0^\infty u^j \nu(\mathrm{d}u), \qquad c_2 = A_1, \quad c_4 = 3A_2, \quad c_6 = 15A_3. \tag{21}$$

This extension could describe several environmental channels or a heterogeneous effective aperture. Its geometric interpretation is not assumed in the mathematical result.

Proposition 2 (Minimum decoherence at fixed mechanical cumulants)**.** *For this class of Gaussian mixtures with $c_2, c_4 > 0$, the rate satisfies, at every separation,*

$$\boxed{\mathcal{R}_{\mathrm{pred}}(d) \;\le\; \mathcal{R}_{\mathrm{mix}}(d) \;\le\; \frac{c_2 d^2}{2\hbar^2},} \tag{22}$$

where the lower expression is Eq. (17). At nonzero separation the lower equality is reached by a single nonzero transfer variance. The corresponding path integrals obey the same ordering.

To see this, set $k = d^2/(2\hbar^2)$ and use the probability measure $w(\mathrm{d}u) = u\nu(\mathrm{d}u)/A_1$. Then

$$\frac{\mathcal{R}_{\mathrm{mix}}}{A_1} = \mathbb{E}_w f_k(u), \qquad f_k(u) = \frac{1 - \mathrm{e}^{-ku}}{u} = \int_0^k \mathrm{e}^{-tu}\mathrm{d}t. \tag{23}$$

For $k > 0$, f_k is strictly convex, so Jensen's inequality gives the lower bound with $\mathbb{E}_w u = A_2/A_1$. The upper bound follows from $1 - \mathrm{e}^{-ku} \le ku$. This proof requires no truncation of the separation expansion.

A complementary extremal question is studied by Piccione [21]: minimizing heating over spatial smearing profiles at fixed smearing variance. In that problem the Gaussian is optimal for GRW, but not for every collapse model. Proposition 2 instead fixes measured c_2, c_4 and minimizes decoherence within positive mixtures of momentum-transfer Gaussians. The constraints, admissible profiles and optimized observables differ; neither optimization implies the other.

The bound sharpens the cross-experiment test. After the same physical channel has been isolated in both measurements, decoherence below the mechanical prediction cannot be explained merely by replacing a single aperture with a positive mixture of Gaussian widths. Greater attenuation is compatible with heterogeneity and must be examined further. Readout noise is not a physical decohering channel and must not be inserted into c_2 in this comparison.

There is also a direct measure of heterogeneity:

$$\eta \equiv \frac{3c_6 c_2}{5c_4^2} = \frac{A_3 A_1}{A_2^2} = 1 + \frac{\mathrm{Var}_w\, u}{(\mathbb{E}_w u)^2} \ge 1, \qquad \frac{r_{M,24}^2}{r_{M,46}^2} = \eta. \tag{24}$$

Thus the two apparent apertures are ordered, $r_{M,24} \geq r_{M,46}$. A related Gaussian-background-insensitive inequality is

$$\frac{5c_8c_4}{7c_6^2} \geq 1. \tag{25}$$

Equality holds for a single width. A significant value below these bounds, under the stated subtraction and stationarity conditions, rules out this whole mixture class rather than selecting a different mean radius. These conclusions do not extend without proof to arbitrary non-Gaussian transfer kernels or correlated event processes.

4.3 From a path formula to a measured harmonic

For symmetric triangular separation, with maximum $d_{\max}$ and total duration T_I,

$$\mathcal{D} = \Gamma_D T_I K_{\triangle}(d_{\max}, r_d), \qquad K_{\triangle} = 1 - \frac{\sqrt{\pi} r_d}{d_{\max}} \operatorname{erf}\left(\frac{d_{\max}}{2r_d}\right). \tag{26}$$

Its small-separation limit is $K_{\triangle} = d_{\max}^2/(12r_d^2) + O(d_{\max}^4/r_d^4)$. A selected interference harmonic with conventional amplitude V_0 has normalized amplitude $\exp(-\mathcal{D})$ within this path model. A near-field apparatus requires the correct harmonic separation, grating propagation and ensemble averaging [22, 23]. The exponent must be applied inside the mass and velocity average, not evaluated at a mean mass after averaging. Appendix C states that distinction explicitly.

Figure 3 gives an independent synthetic test of this forward calculation. The mechanical sample alone determines the prediction band; the coherence counts are generated with a separate seed and are never used to refit it. At the reference design, mechanics gives $r_M = 24.86 \pm 0.78\,\mathrm{nm}$ and $\Gamma_M = 8.87 \pm 0.54\,\mathrm{s}^{-1}$. The independent resolving scan gives $r_I = 25.52 \pm 0.49\,\mathrm{nm}$ and $\Gamma_I = 9.19 \pm 0.16\,\mathrm{s}^{-1}$ (one-standard-error estimates). Propagating the full mechanical covariance gives a prediction-residual statistic $Q = 6.63$ for eight entries, with approximate $p = 0.58$. These numbers validate the simulated inference chain; they are not a fit to an observed localization signal.

5 The three-way reconstruction of a common aperture

5.1 An activation measurement with a distinct inference role

The activation radius is the scale at which the normalized rate $\Gamma_D/(M/m_0)^{\alpha}$ turns from a power law towards saturation. For fixed density and fixed shape, $M \propto R^3$, so

$$\frac{\mathrm{d}\ln\Gamma_D}{\mathrm{d}\ln R} = 3\alpha + \frac{p}{1 + (R/r_A)^p}. \tag{27}$$

The $7 \to 3$ reference slopes follow for $\alpha = 1$, $p = 4$ [3]. The midpoint occurs at $R = r_A$. In an actual analysis it is preferable to fit the complete rate or count model rather than differentiating noisy rate estimates.

The asymptotes also identify what cannot be learned from a restricted scan. If all bodies satisfy $R \ll r_A$, the amplitude contains the degenerate product $\gamma_0 r_A^{-p}$. If all satisfy $R \gg r_A$, the activation radius has little influence. A scan must span the crossover. Fitting both α and p additionally requires enough dynamic range, and independent mass or density variation is useful for separating mass amplification from size activation. The reference numerical calculation fixes these exponents; it does not establish them.

For the common-aperture comparison, define $\boldsymbol{\ell} = (\ln r_M, \ln r_I, \ln r_A)$ and its covariance Σ. An asymptotic compatibility statistic is

$$Q_A = \min_{\ell_*} (\boldsymbol{\ell} - \ell_* \mathbf{1})^{\mathsf{T}} \Sigma^{-1} (\boldsymbol{\ell} - \ell_* \mathbf{1}). \tag{28}$$

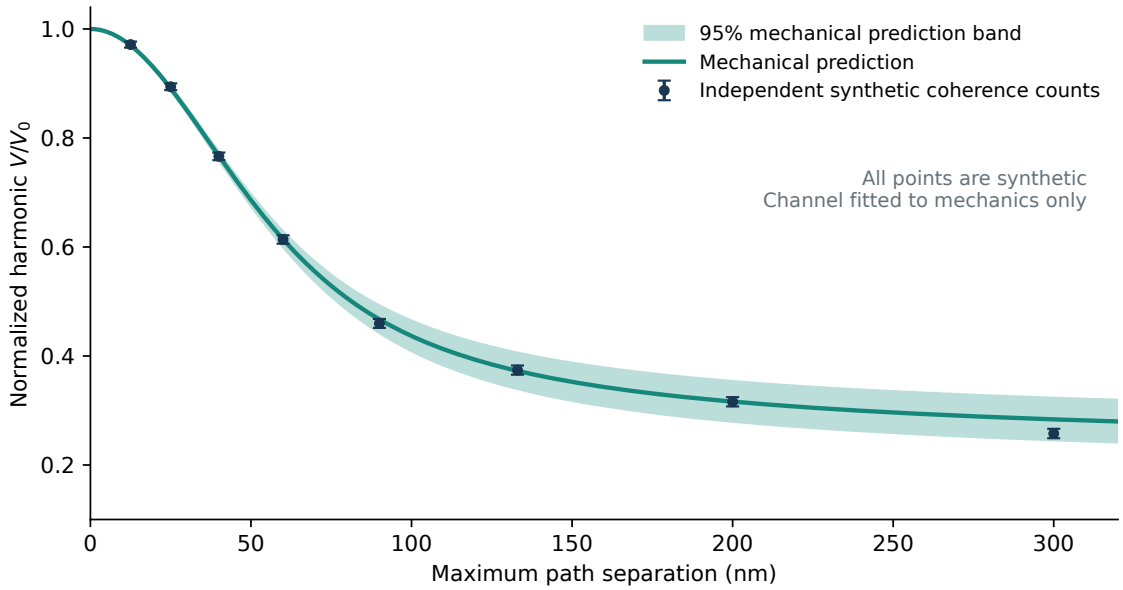


Figure 3: Coherence predicted from mechanical data without refitting the localization parameters. The shaded region propagates the joint mechanical parameter covariance. Independent synthetic binomial counts measure a single harmonic for triangular separation histories; point error bars are one standard error. The assumed conventional contrast is $V_0 = 0.8$, known here by construction. This is an idealized signal model, not a reproduction of a specific grating experiment.

With three identifiable Gaussian estimates and known covariance, it has approximately two degrees of freedom under a common aperture. Shared mass, size and displacement calibrations produce off-diagonal elements of Σ. Separate data sets do not justify discarding them. Near parameter boundaries or with weak signals, a parametric simulation of the complete comparison is preferable to the Gaussian approximation.

5.2 A controlled independent-reconstruction example

The activation example uses radii from 10 to 48 nm, known masses at a stated density, fixed exponents $(1, 4)$ and separate simulated counts. An idealized constant-separation signal at $d = 300\,\mathrm{nm}$ probes the rate close to saturation. Exposure times are selected in advance from the reference model to keep attenuation of order one, and remain fixed in each fit. The resolving correction is retained; at $r_d = 25\,\mathrm{nm}$ it differs from unity by e^{-36}. These features make the fitted activation radius effectively independent of the resolving length within this design.

The compatible sample gives $r_A = 25.29 \pm 0.16\,\mathrm{nm}$. Together with the independently reconstructed mechanical and interference radii, Eq. (28) gives $Q_A = 0.52$, with approximate $p = 0.77$. A second activation sample is generated with $r_A = 35\,\mathrm{nm}$ while retaining $r_I = r_M = 25\,\mathrm{nm}$. Its fit gives $35.05 \pm 0.31\,\mathrm{nm}$ and $Q_A = 304.3$. Each individual response remains well described by its own model; the common-length identification fails. Figure 4 displays both cases.

This calculation establishes statistical identifiability for explicitly specified observables. The activation exposures range from 60 ms down to 14.6 μs. Preparing a 300 nm separation and maintaining the prescribed signal at those short times is an additional experimental requirement, not a capability established by the simulation. Section 6 quantifies why the activation crossover cannot simply be inserted into the reference Talbot geometry at the upper normalization.

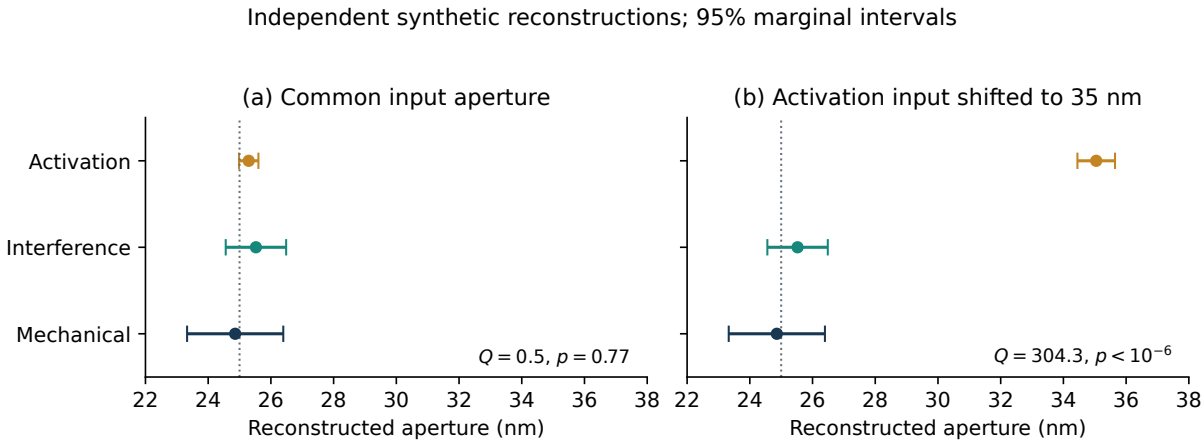


Figure 4: A common-aperture comparison can succeed or fail even when the individual fits are identifiable. All reconstructions are synthetic. Mechanical and interference data are shared between panels; independent activation data have a generating radius of (a) 25 nm or (b) 35 nm. Horizontal bars are 95% marginal intervals. The compatibility statistics use log radii and the covariance assumed in the synthetic design. Exact calibrations here remove shared systematic correlations; a real experiment must restore them.

Table 1: Reference channel and free-flight design. Values follow from the stated model inputs.

Quantity	Value
Domain mass M	1.87668 MDa
Flight duration T	0.166386 s
Activation $F_4(R/r_d)$	0.0176315
Rate Γ_D; occupancy λ	9.01221 s^{-1}; 1.49950
One-axis transfer rms σ_q	2.98278×10^{-27} kg m s^{-1}
Added position rms $\sqrt{\kappa_2^{X,D}}$	112.59 nm
Channel excess kurtosis: momentum; position	2.00066; 3.60119
Triangular exponent at $d_{\max} = 133$ nm	1.00000

6 An experimental window where the event statistics remain visible

6.1 Reference scale and conditional normalization

The quantum companion obtained a central normalization ceiling $\gamma_0 = 2.72366 \times 10^{-4}\,s^{-1}$ at $r_d = 25$ nm and $\alpha = 1$, conditional on each LISA Pathfinder test mass being a saturated rigid domain, independent channel forces on the two masses, and a white transfer spectrum over the relevant comparison [3]. Its input is the corrected acceleration amplitude 1.74 ± 0.05 fm $s^{-2}/\sqrt{\text{Hz}}$ [24]. This is a conditional upper normalization, not a detected channel or a confidence bound from a joint likelihood. We use it as one declared design point.

At density 971 kg m^{-3}, diameter 18.30095 nm and grating period $d_g = 133$ nm, the reference first-order exposure is $T = 2Md_g^2/h$. Table 1 collects the resulting quantities. The 25 nm aperture and 18.3 nm body diameter are model and protocol inputs; neither is a universal quantum–classical threshold. Current matter-wave experiments provide relevant scale benchmarks [14, 15], while levitated optomechanics supplies complementary tools for low-dissipation force sensing, state preparation and nanoparticle control [25, 26]. Precision mechanical searches for stochastic localization also show that excess-force backgrounds can be constrained quantitatively [16, 17, 18]. These capabilities are complementary rather than already integrated: the reference design is not an existing mechanical measurement of the interfering particles, and no present apparatus is assumed to realize the complete three-route test.

6.2 An exact distribution likelihood for free-flight readout

Let $q_0 = \hbar/(\sqrt{2}\,25\,\mathrm{nm})$ be a reference unit, $x = X/(q_0 T/M)$ and $a = \sigma_q/q_0$. The symbol a here is a scale parameter, unrelated to a cosmological scale factor. With dimensionless Gaussian variance b from propagated preparation and readout, the characteristic function is

$$\Phi_x(k) = \exp\left[-\frac{bk^2}{2} + \lambda\{J(ak) - 1\}\right], \quad J(z) = \int_0^1 \mathrm{e}^{-z^2u^2/2}\mathrm{d}u = \frac{\sqrt{\pi/2}}{z}\,\mathrm{erf}(z/\sqrt{2}), \tag{29}$$

with $J(0) = 1$. This follows by averaging the impulse time over the flight. It includes events at all flight times and the no-event component, convolved with the initial state and measurement response. Fourier inversion supplies a normalized density. We maximize its likelihood over $(\ln\lambda, \ln a)$, which leaves both the rate and aperture free even though q_0 defines the unit.

The reference synthetic experiment uses $N = 30\,000$ independent preparations, $b = \lambda/3 = 0.499835$ and true $a = 1$. The background variance b is held fixed at its generating value throughout the likelihood fits and precision forecasts; no finite calibration uncertainty is included in these numerical results. Thus the Gaussian background and channel contribute equal position variances. An assumed 20 nm rms readout is included in that background. The equivalent propagated preparation rms is 110.8 nm; one pure, uncorrelated Gaussian realization starts with position rms 107.7 nm and momentum rms $4.90 \times 10^{-28}\,\mathrm{kg\,m\,s^{-1}}$. These are required inputs for the example, not demonstrated preparation specifications.

The exact-density likelihood predicts a 3.15% relative aperture precision at this design, compared with 4.02% from second and fourth cumulants alone. In 200 independent synthetic repetitions, the observed standard deviations of log aperture are 3.23% and 4.32%, respectively; all moment reconstructions remain positive. Nominal 95% likelihood intervals cover the input log aperture in 191 of 200 repetitions and the input log rate in 189 of 200. The binomial Monte Carlo uncertainty of a 95% coverage fraction at this sample size is about 1.5 percentage points. These checks support the asymptotic precision estimate locally, without establishing robustness to unknown backgrounds.

6.3 Why large intrinsic kurtosis is not sufficient

For an independent Gaussian background with variance B and channel variance S, define

$$\epsilon = \frac{S}{S+B}. \tag{30}$$

The measured excess kurtosis is reduced to

$$g_{2,P}^{\mathrm{obs}} = \frac{3}{\lambda}\epsilon^2, \qquad g_{2,X}^{\mathrm{obs}} = \frac{27}{5\lambda}\epsilon^2. \tag{31}$$

Knowing and subtracting the mean background variance does not remove its sampling fluctuations. In the background-dominated regime the trials required for a fixed fractional aperture precision grow as ϵ^{-4}. An intrinsically conspicuous non-Gaussian channel can therefore be practically invisible after preparation and readout convolution.

Table 2 uses the exact asymptotic covariance through the eighth moment, and an independent Fisher calculation for the full position density. The numbers are precision forecasts, not discovery significances or guaranteed finite-sample coverage. They assume that B and the instrument scales are known. Uncertain calibration must be included in a joint likelihood; a separate Gaussian background control of N_B independent shots has fractional variance uncertainty approximately $\sqrt{2/N_B}$.

The distinction between precision and attribution is essential. A precise non-Gaussian distribution could originate from gas impacts, optical recoils or intermittent technical forces. The likelihood used here tests what can be learned if the stipulated channel and background model describe the experiment. The intervention tests in Section 7 address the physical attribution.

Table 2: Trials for 10% aperture precision at $\lambda = 1.4995$, with known Gaussian background. Moment entries follow exact asymptotic cumulant covariances; likelihood entries are Fisher forecasts for free-flight position.

ϵ	Momentum moments	Position moments	Position likelihood
1.0	2.29×10^3	2.11×10^3	—
0.5	7.66×10^3	4.85×10^3	2.98×10^3
0.2	1.20×10^5	4.58×10^4	4.52×10^4
0.1	1.60×10^6	5.23×10^5	5.18×10^5

6.4 A quantum preparation budget and a mass cancellation

For a centered initial Gaussian state with position variance V_X, momentum variance V_P and zero symmetrized covariance, free propagation gives

$$B_{\mathrm{prep}}(T) = V_X + \frac{T^2}{M^2} V_P \geq \frac{\hbar T}{M}. \tag{32}$$

The minimum follows from $V_X V_P \geq \hbar^2/4$ and is attained by a pure Gaussian with $V_X = \hbar T/(2M)$. This is a bound within the stated zero-covariance preparation class. Correlated or focused states can have a smaller variance at a selected final time and require their own preparation and readout model; Eq. (32) is not a universal free-mass measurement limit. Contractive quantum states provide an explicit precedent for this distinction [27].

The ratio of channel displacement variance to this preparation scale is

$$\chi \equiv \frac{\kappa_2^{X,D}}{\hbar T/M} = \frac{\Gamma_D \hbar T^2}{6 M r_d^2}, \tag{33}$$

$$\chi\big|_{\alpha=1} = \frac{\gamma_0 \hbar T^2}{6 m_0 r_d^2} F_p(R/r_d). \tag{34}$$

Linear mass amplification cancels the explicit mass in this signal-to-preparation comparison. The remaining size dependence is activation. This connects the collective law to an experimentally meaningful quantum preparation budget. For general α, the uncancelled factor is $M^{\alpha-1}/m_0^{\alpha}$.

At the reference point, $\chi = 2.2515$ and the minimum propagated preparation rms is 75.04 nm. With independent readout variance σ_{ro}^2 and no other background,

$$\epsilon \leq \frac{\chi}{1 + \chi + M\sigma_{\mathrm{ro}}^2/(\hbar T)}. \tag{35}$$

The assumed $\epsilon = 0.5$ lies below this bound, so the synthetic preparation is consistent with quantum uncertainty. Achieving it for the chosen material is a separate engineering task. Ground-state cooling of levitated particles demonstrates relevant control methods [26], but ground-state occupation in a stiff trap alone does not meet a specified free-flight momentum width. For orientation, the reference channel momentum variance corresponds to $S_P/(Mk_B) = 0.310\,\mathrm{nK}$; this is a variance-equivalent scale, not the particle's internal temperature or a claim of thermal equilibrium.

For a saturated domain at the reference normalization, $\chi = 1$ corresponds to $T = 14.72\,\mathrm{ms}$. At the weakly activated reference radius it requires $T = 110.9\,\mathrm{ms}$. This is a preparation crossover, distinct from the coherence boundary. Moreover, for a first-order exposure $T = 2Md_g^2/h$,

$$\chi = \frac{\lambda d_g^2}{6\pi r_d^2}. \tag{36}$$

At fixed occupancy and fixed grating-to-aperture ratio, this budget is independent of mass. A lower normalization may move the same occupancy to a larger body and longer flight without improving this dimensionless ratio.

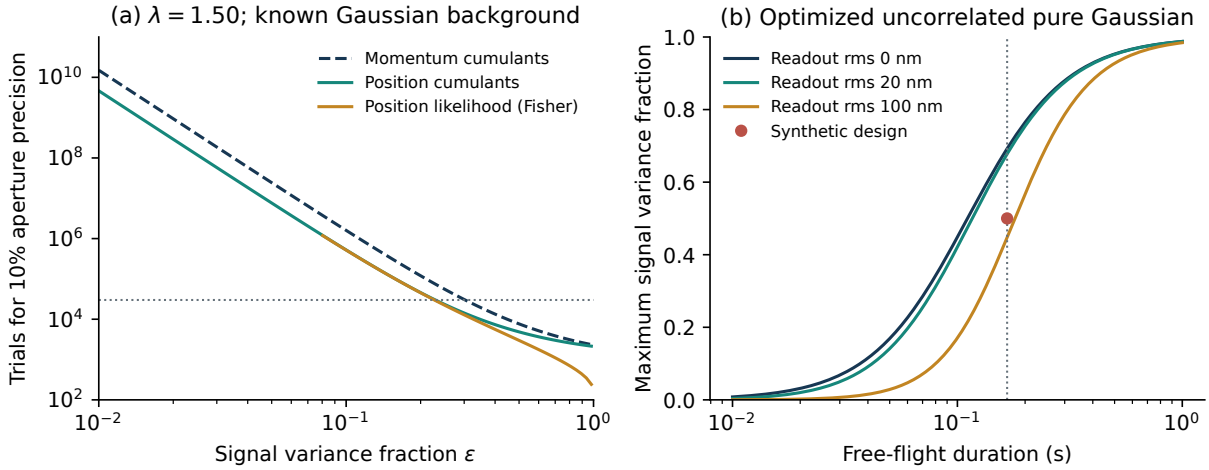


Figure 5: Sensitivity and physical preparation budget. (a) Asymptotic trials for 10% aperture precision versus the channel fraction of the total variance. The horizontal line marks 30 000 trials; the exact-density likelihood improves on moments where the distribution shape is informative. (b) Maximum fraction permitted within the optimized zero-covariance pure-Gaussian preparation class at the reference mass and rate, for three assumed readout errors and no environmental diffusion. The synthetic reference point is below the corresponding bound. These curves describe requirements, not certified apparatus performance.

6.5 Size, time, repetition and the activation crossover

Thirty thousand reference free flights require at least $NT = 4.99 \times 10^3$ s of exposure, about 1.39 hours for a serial experiment before preparation, recapture and dead time. Correlations between trials reduce the effective sample count. The characteristic event rate is about $9\,\mathrm{s}^{-1}$, but a terminal-position measurement does not need to time-resolve each event; it must maintain a calibrated impulse response over the flight. A finite readout window changes that response. For example, a 1 ms terminal averaging window changes the second and fourth channel cumulants by approximately 0.9% and 1.5% at this flight duration; Appendix B gives the exact correction.

The activation turnover probes a different experimental demand. A compact body with $R = r_d = 25$ nm has mass 38.27 MDa at the reference density. At the same normalization its rate is $5.21 \times 10^3\,\mathrm{s}^{-1}$, whereas a first-order 133 nm Talbot exposure is 3.39 s. The occupancy is then 1.77×10^4, so resolved-path coherence is extinguished in that configuration. The turnover cannot be tested merely by increasing the particle size while retaining all other settings.

Two quantitatively distinct options follow. A protocol with exposure of order $1/\Gamma_D \simeq 0.192$ ms could probe the rate at the turnover, provided preparation and path separation can be realized that quickly. Alternatively, at that size and Talbot exposure, occupancy 1.5 requires $\gamma_0 \simeq 2.31 \times 10^{-8}\,\mathrm{s}^{-1}$, well below the reference ceiling and with a much longer flight than the 18.3 nm-diameter design. The broad activation scan in Figure 4 is consequently an identifiability calculation for a future rate-measurement protocol. A single currently demonstrated apparatus is not asserted to implement all three routes.

Decreasing γ_0 at fixed mass and exposure decreases the signal fraction as well as the occupancy. It does not guarantee easier detection because intrinsic kurtosis increases. In the weak-channel, fixed-background limit, the observed fourth cumulant tends to zero with γ_0 and the information about r_d disappears. A non-detection therefore constrains the accessible (γ_0, r_d) region; it cannot exclude a theory with arbitrarily small allowed normalization unless another physical requirement supplies a nonzero lower bound.

6.6 A fixed-apparatus map of the reconstructible region

The precision calculation can be extended across (γ_0, r_d) while keeping the apparatus fixed. We retain the reference mass, material radius, flight time, $N = 30\,000$ trials and dimensionless background variance $b = 0.499835$. The true transfer scale becomes $a = (25\,\mathrm{nm})/r_d$ and the occupancy is obtained from Eq. (3), with $(\alpha, p) = (1, 4)$. The background is not reset to equal the changing signal. At every point, both the rate and width remain free in the inference. The plotted quantity is

$$s_r = \sqrt{\left[(NI)^{-1}\right]_{\ln a, \ln a}} = \sigma_{\mathrm{Fisher}}(\ln r_d), \tag{37}$$

where I is the information per mechanical trial from the exact convolved density. This is a local asymptotic precision forecast with an exactly known background, not a detection contour. At 30%, a log-radius standard deviation is only approximately a fractional radius error. Appendix D.3 supplies analytic score derivatives and convergence checks.

Figure 6 overlays two physically distinct conditional boundaries. With the saturated-test-mass, white-spectrum and linear-amplification assumptions retained, the LPF ceiling scales as

$$\gamma_{\mathrm{LPF}}(r_d) = 2.72366 \times 10^{-4} \left(\frac{r_d}{25\,\mathrm{nm}}\right)^2 \mathrm{s}^{-1}. \tag{38}$$

An illustrative lower requirement is obtained by demanding that a sphere of radius $R_{\mathrm{cl}} = 1\,\mu\mathrm{m}$, at the reference density, suppress coherence at separation $d_{\mathrm{cl}} = 1\,\mu\mathrm{m}$ to $\varepsilon_{\mathrm{cl}} = 10^{-6}$ in $T_{\mathrm{cl}} = 1\,\mathrm{ms}$ [3]:

$$\gamma_{\mathrm{cl}}(r_d) = \frac{-\ln \varepsilon_{\mathrm{cl}}}{(M_{\mathrm{cl}}/m_0) F_4(R_{\mathrm{cl}}/r_d) T_{\mathrm{cl}} [1 - \mathrm{e}^{-d_{\mathrm{cl}}^2/(4r_d^2)}]}, \quad M_{\mathrm{cl}} = \frac{4\pi\rho R_{\mathrm{cl}}^3}{3}. \tag{39}$$

This is a chosen operational classicality criterion, not a universal theoretical or observational lower bound. It must be recalculated if the macroscopic criterion changes.

At $r_d = 25\,\mathrm{nm}$, the 10% and 30% contours occur at $\gamma_0 = 2.25 \times 10^{-5}$ and $4.20 \times 10^{-6}\,\mathrm{s}^{-1}$, respectively. The latter is about 65 times below the reference ceiling. The aperture can therefore remain locally identifiable well below that ceiling under the declared calibration assumptions. At the illustrative floor, $\gamma_{\mathrm{cl}} = 5.64 \times 10^{-9}\,\mathrm{s}^{-1}$, the same apparatus instead produces only $N\lambda = 0.932$ channel events on average across all trials, with probability $\mathrm{e}^{-N\lambda} = 0.394$ of no events. This explains a concrete limit of that apparatus, rather than exclusion of the whole allowed normalization range.

The reference Monte Carlo validates precision locally near its generating point; it does not validate coverage across this map. Unknown or drifting background, imperfect scale calibration and finite-sample boundary effects require the joint inference described in Appendix D. Regions with fewer than ten expected events over the entire data set are left uncoloured to avoid implying a regular reconstruction there. This display rule is not a sufficient statistical-validity criterion for the remaining points.

6.7 A staged experimental programme

The common-aperture hypothesis does not require that all three reconstructions be attempted simultaneously. A more robust strategy is staged, so that each step has a distinct failure criterion and supplies calibrated inputs to the next one. Table 3 summarizes the logical sequence. A later gravitational-state test is a fourth layer rather than a prerequisite for Stages I–III: it must predict how the reconstructed width changes between independently specified geometric states. This ordering prevents a failed mechanics–coherence comparison from being hidden by retuning the activation law, and prevents a failed activation comparison from being absorbed into a post-hoc change of domain definition. The first useful experimental result can therefore be a null or inconsistency result, provided the calibrated sensitivity is sufficient to exclude the corresponding region of parameter space.

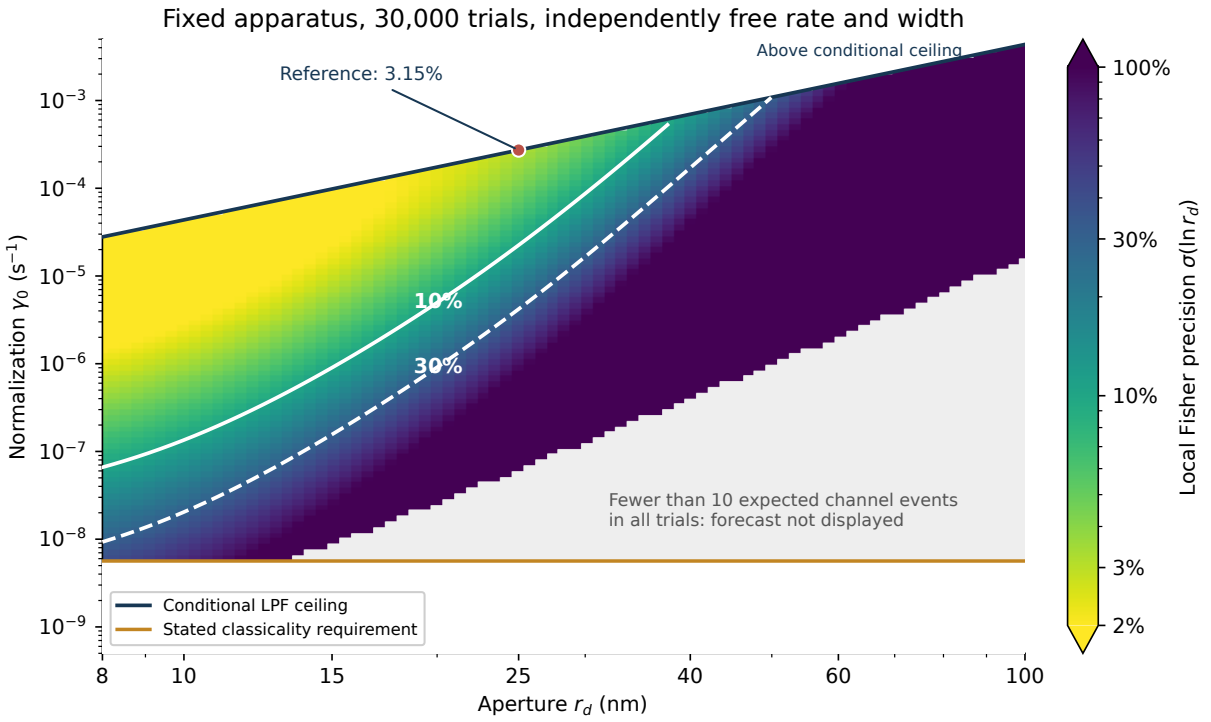


Figure 6: Aperture precision for the fixed reference apparatus, with free rate and width and exactly known Gaussian background. White solid and dashed curves mark $\sigma(\ln r_d) = 0.10$ and 0.30. The red point is the original synthetic design. The upper boundary is the conditional central LPF ceiling; the lower boundary is the explicitly chosen macroscopic classicality requirement. Grey denotes fewer than ten expected channel events in 30 000 trials. Colour is capped at 2% and 100%; values beyond those limits occupy the end colours. These are Fisher forecasts, not measured exclusions or established finite-sample confidence intervals.

Table 3: Staged implementation of the common-aperture test. Each stage can fail independently; later stages test the earlier channel estimate with its full uncertainty, without refitting it to the test data.

Stage	Primary observable	Required control	Decisive outcome
I: mechanics	Full displacement or filtered-force distribution	Calibrated impulse response; pressure, optical and temperature controls; prespecified tail handling	Recover r_M, Γ_M; test the c_6, c_8 hierarchy where statistically resolved.
II: coherence	Independent interference harmonic versus separation	Carry the joint mechanical parameter distribution forward without refitting the localization channel; propagate mechanical, apparatus and conventional-contrast uncertainties	Test the blind coherence prediction and the lower bound in Eq. (22).
III: geometry	Size-dependent activation across the crossover	Fixed domain convention, mass/size calibration and adequate dynamic range	Test $r_A = r_I = r_M$; a reliable mismatch rejects the common-length identification.

7 Distinguishing a geometric channel from ordinary fluctuations

7.1 Interventions that address the origin of the signal

Residual gas impacts and photon recoils are momentum-transfer processes, and their coherence effects are governed by the same general correspondence [5, 6]. Consequently, successful prediction of coherence from mechanics establishes a shared transfer channel, but does not alone

identify its origin. Pressure, optical intensity and internal-temperature interventions are integral parts of the test.

At fixed material state, a pressure scan can estimate the component that scales with residual-gas density. Controlled illumination varies optical recoils. A temperature scan probes thermal emission and absorption, provided it does not change the bound-domain rigidity or material size. These are not merely formal controls: pressure scans have quantitatively isolated collisional decoherence, and controlled molecular heating has isolated thermal-radiation decoherence in matter-wave interferometers [12, 13]. Repeated exposures test the predicted linear cumulant growth in momentum and the T^{2n+1} law in free-flight position. A directional measurement tests isotropy after the full instrument response is accounted for. Each intervention should be predicted by an explicit environmental model rather than assigned an arbitrary residual amplitude at every setting.

Gaussian technical fluctuations change c_2 and dilute the measured kurtosis. Intermittent technical impulses can also change c_4, c_6 and imitate the finite-event channel. The observed distribution must therefore be compared across apparatus settings, domain preparations and detectors. Rejecting large excursions as outliers without a prespecified detector-failure rule would remove precisely the information on which the aperture reconstruction relies.

7.2 Model comparisons and exact degeneracies

Three nested diagnostic comparisons are useful. A Gaussian diffusion model can match the measured variance, but predicts no added cumulants above second order and only quadratic separation dependence. The finite Gaussian channel fixes a hierarchy and a saturating resolving curve. A positive mixture of Gaussian widths has additional freedom, yet still obeys Eqs. (22), (24) and (25). These are calculable alternatives with progressively different observable constraints, not labels assigned to an unexplained excess.

A competitor producing exactly Eq. (5) with the same domain scaling is observationally identical for all experiments considered here. In particular, a matching localization model cannot be separated merely by renaming its length a geometric aperture. Extended-body CSL comparisons require their actual mass-density form factors and regime of validity [8, 28]; modern non-interferometric searches likewise emphasize explicit mechanical response functions and environmental attribution rather than an unexplained residual-noise label [16, 17, 18]. The DJAMILAR-specific test adds the activation law, the physical domain rule and the identification with a gravitational collective state. Those extra commitments must supply independent information if they are to discriminate between identical effective channels.

The aperture equality is falsifiable within its declared realization: a reliable disagreement between r_A, r_I, r_M rejects the common-length identification at the state tested. A failure of the mechanical hierarchy first challenges the assumed kernel or isolation procedure. Decoherence below the lower bound rejects the Gaussian-mixture explanation of that isolated noise channel. These outcomes identify which physical bridge has failed. They do not justify changing the domain or adding an environment-dependent normalization after seeing the discrepancy without treating the change as a new model.

7.3 A calculable extended-body CSL alternative

The mass-density form factor supplies a concrete way to distinguish two generators that agree in the point-body limit. Consider standard nondissipative, mass-proportional CSL with Gaussian spatial smearing, a rigid homogeneous sphere of radius R, and the continuous-density approximation [19]. For isotropic centre-of-mass transfers, its rate measure has shape

$$\nu_{\mathrm{CSL}}(\mathrm{d}^3q) \;\propto\; \mathrm{e}^{-r_C^2 q^2/\hbar^2}\,|F(qR/\hbar)|^2\,\mathrm{d}^3q, \qquad F(z)=\frac{3(\sin z - z\cos z)}{z^3}, \quad F(0)=1. \tag{40}$$

Table 4: CSL form-factor diagnostics from Eq. (41). Rounded values; the full quadrature table is provided with the code.

R/r_C	$r_{M,24}/r_C$	$r_{M,46}/r_C$	η
0.3	1.0090	1.0091	0.99995
1.0	1.1044	1.1074	0.99453
2.0	1.4302	1.4524	0.96962
3.0	1.7859	1.6190	1.21677
5.0	2.0638	1.5667	1.73525
10.0	2.1918	1.5376	2.03191

The explicit Gaussian convention fixes the point-limit axial variance to $\hbar^2/(2r_C^2)$. Finite-body form factors are also central to optomechanical collapse searches [29]; the present comparison retains higher transfer moments rather than only the diffusion coefficient.

Set $\xi = R/r_C$ and $k = qr_C/\hbar$. Angular averaging gives the dimensionless integrals

$$J_n(\xi) = \frac{1}{2n+1}\int_0^\infty k^{2n+2}\mathrm{e}^{-k^2}F(\xi k)^2\mathrm{d}k, \qquad c_{2n} = \mathcal{A}\left(\frac{\hbar}{r_C}\right)^{2n} J_n, \tag{41}$$

where the common positive prefactor $\mathcal{A}$ has units of inverse time. Its mass and normalization dependence cancels from the diagnostics

$$\frac{r_{M,24}}{r_C} = \sqrt{\frac{3J_1}{2J_2}}, \qquad \frac{r_{M,46}}{r_C} = \sqrt{\frac{5J_2}{2J_3}}, \qquad \eta_{\mathrm{CSL}} = \frac{3J_3J_1}{5J_2^2} = \left(\frac{r_{M,24}}{r_{M,46}}\right)^2. \tag{42}$$

Outside the point-body limit these are *effective reconstructed radii*: applying the single-Gaussian inverse does not make either radius equal to the underlying CSL parameter r_C. All quantities in Eq. (42) are dimensionless, and no event-rate calibration is needed for their population ratios.

The result is non-monotonic and more informative than a simple broadening. The Gaussian-mixture inequality $\eta \geq 1$ is violated near the sphere-size crossover: numerical quadrature gives $\eta_{\min} = 0.967160$ at $\xi = 1.86848$, a maximum deficit of 3.284%, followed by a return to unity at $\xi = 2.29745$. There is no finite lower onset of this deficit, since

$$\eta_{\mathrm{CSL}} = 1 - \frac{\xi^4}{175} + O(\xi^6) \quad (\xi \to 0). \tag{43}$$

For large sharp-boundary spheres, a different diagnostic remains:

$$\frac{r_{M,24}}{r_C} \longrightarrow \sqrt{5}, \qquad \frac{r_{M,46}}{r_C} \longrightarrow \sqrt{\frac{7}{3}}, \qquad \eta_{\mathrm{CSL}} \longrightarrow \frac{15}{7}. \tag{44}$$

Appendix E derives these limits. Figure 7 and Table 4 display the intermediate regime. Thus the first inferred radius saturates at large size, while the two reconstructions retain a finite mismatch.

This suggests a size-dependent kernel test, with the impulse response and backgrounds calibrated separately at each size. DJAMILAR's single-width realization predicts the same reconstructed width and $\eta = 1$ throughout a fixed geometric state; this CSL realization predicts Eq. (42). A scan spanning $R \sim r_C$ tests the characteristic size dependence. Two sizes both deep in the point limit supply little form-factor discrimination; two large sizes likewise show little further drift, although the higher-cumulant mismatch remains. A resolved value $\eta < 1$ rejects both a single Gaussian and its positive width-mixture extension. Conversely, $\eta > 1$ alone does not distinguish extended-body CSL from a Gaussian mixture.

The required precision of c_6 and of η must be assessed independently; the 3.2% reference precision on r_M does not establish sensitivity to a 3.3% deficit in η. Surface structure, internal motion, non-Gaussian smearing or dissipative CSL require recalculating Eq. (40). Even a successful shape discrimination would identify an effective generator, not establish a unique microscopic origin.

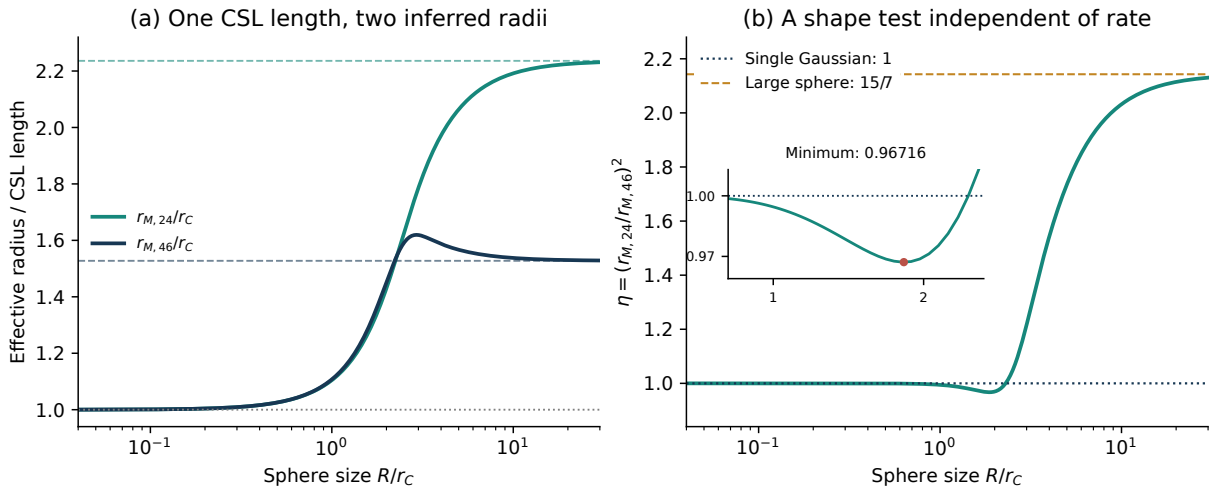


Figure 7: Theoretical diagnostics for standard Gaussian-smearing CSL of a homogeneous, sharp-boundary sphere. (a) Two applications of the Gaussian inverse to the CSL cumulants yield different effective radii. Dashed lines show their large-sphere limits. (b) The rate-independent ratio η first falls below the positive-Gaussian-mixture bound, then approaches $15/7$. The inset resolves its 3.284% maximum deficit. The single-width DJAMILAR kernel predicts $\eta = 1$ at every size in its rigid-domain regime. No experimental error bars are asserted here.

8 From a measured localization length to the gravitational state

Equation (2) gives a precise entry point into the wider programme. For two states,

$$\Delta\vartheta = 2\ln\frac{r_{d,2}}{r_{d,1}} + \ln\frac{n_{d,2}}{n_{d,1}}. \tag{45}$$

If the proper surface density is fixed, a ratio of reconstructed apertures measures half the change in the collective state. The measurement is an operational constraint on this identification. It does not independently determine the microscopic density or the absolute reference of ϑ.

For a fixed domain, fixed exponents and fixed γ_0, the common-aperture law predicts

$$\delta\ln\Gamma_D = -p(1-F_p)\delta\ln r_d, \qquad \delta\ln c_{2n} = -[p(1-F_p)+2n]\delta\ln r_d. \tag{46}$$

In particular, $\delta\ln(c_4/c_2) = -2\delta\ln r_d = -\delta\vartheta$ at fixed density. This ratio removes the rate normalization. It can constrain a state variation even if the total rate also responds to an independently characterized normalization change. If γ_0 itself varies with state, the absolute-rate prediction in Eq. (46) must include that derivative; the adjacent-cumulant ratio remains the more direct width diagnostic.

To turn this into a gravitational test, one must first calculate $\Delta\vartheta$ from the dynamical representative, the matter sources and the relevant boundary conditions, including the transfer from any large-scale state to the local experiment [2]. Neither a local Newtonian potential nor a cosmological drift may simply be substituted for that calculation. The representative does not assert a universal $G_N \propto r_d^2$, and its Einstein coefficient is not inferred from the localization radius. No variation of Newton's constant is derived here.

There are concrete precedents for connecting localization to a classical gravitational field. Tilloy's massive-flash GRW model uses localization events as Newtonian sources [30]. The gravitational Poissonian spontaneous localization framework also couples localization and gravitational feedback; recent work explicitly allows different smearing lengths for those two operations [31]. These constructions clarify what DJAMILAR's common-length identification adds: equality of the relevant scales must be predicted and tested, rather than following automatically from a stochastic gravitational mechanism. Their Poisson structure alone does not establish Eq. (5);

applying our Gaussian inverse to a full feedback dynamics requires first deriving its effective transfer generator and checking its spatial homogeneity and independence assumptions.

Oppenheim et al. derive a different, complementary constraint: consistent classical–quantum coupling relates decoherence of the quantum system to diffusion of the classical gravitational variables [32]. That classical phase-space diffusion is not the matter momentum diffusion measured by c_2 here. Their trade-off therefore cannot be identified with either side of Eq. (22). A DJAMILAR completion formulated as such a hybrid dynamics would need to specify the classical variables, coupling and backreaction before that constraint could be applied.

This limited bridge is nevertheless useful. It specifies the new observable that a completed gravitational calculation must predict: a change in an independently reconstructed transfer width, cross-checked by activation and interference. The stochastic energy increase also remains a matching obligation for a closed microscopic completion; the effective open-system channel by itself does not provide its reservoir or a complete backreaction law.

9 Conclusions: independent tests of a common geometry

The proposed common aperture becomes experimentally meaningful when it is reconstructed in more than one way. We have derived a mechanical inverse that separates localization rate and length, propagated it to a coherence prediction with fixed channel parameters, and defined the subsequent comparison with size activation. These results extend the second-moment coherence–noise relation by retaining information carried by the shape of the fluctuation distribution.

The Gaussian-mixture extension yields a further result: the single-aperture channel is extremal. Its coherence loss is a lower bound at fixed second and fourth mechanical cumulants, and unequal Gaussian widths impose an ordered hierarchy of inferred radii. A discrepancy can therefore reject a class of effective channels instead of merely demanding another fitted length.

The numerical calculation shows what is required to resolve this information. For a declared 0.166 s free-flight design with a Gaussian background of known variance equal to the channel contribution, 30 000 synthetic trials give approximately 3.2% aperture precision. This is a conditional parameter-precision result, not a discovery significance or a robustness claim against unknown backgrounds; stronger background dilution causes a steep loss of information. The quantum preparation budget exposes a mass cancellation for linear amplification and distinguishes a mechanics-sensitive window from an activation-turnover experiment. The latter requires a separate exposure and preparation strategy at the reference normalization.

The extended-body CSL calculation makes the kernel comparison quantitative. A homogeneous sphere produces two different effective radii, a shallow violation of the Gaussian-mixture inequality near $R \sim r_C$, and the asymptotic ratio $\eta = 15/7$. These are rate-independent predictions of the specified competitor, while the single-width DJAMILAR channel gives $\eta = 1$. Their use requires a dedicated higher-cumulant uncertainty calculation and control of body shape. The fixed-apparatus map adds a separate result: at 25 nm, 30% local aperture precision extends to a normalization about 65 times below the reference ceiling under exactly known background. Neither this precision contour nor the CSL diagnostic is an observed signal.

The staged programme in Table 3 makes the next research tasks explicit. First, implement and calibrate a free-flight or filtered-mechanics protocol against non-Gaussian environmental controls, using the complete distribution and its measured response. Second, carry its inferred channel and covariance into an independently recorded coherence signal, with no localization refit. Third, construct a crossover-spanning activation protocol. In parallel, an independent gravitational state-transfer calculation should predict how the reconstructed aperture changes between specified source and boundary configurations. Its comparison with experiment forms a further test and must not be adjusted to repair an earlier failed cross-prediction. Their purpose is concrete: establish whether a single physical length really connects the responses attributed to DJAMILAR.

The programme gains explanatory force only insofar as those independent constraints can be satisfied together, and it remains falsifiable if any one of the calibrated cross-comparisons fails.

Data and code availability. All numerical observations in this article are synthetic. The accompanying archive contains the source manuscript, figures, generated samples, count tables, CSL quadrature results, fixed-apparatus Fisher forecasts, numerical validation, random seeds and executable reproduction scripts. It contains no newly collected experimental data. The three prior DJAMILAR works are cited to their Research Square preprint records; these records are not peer-reviewed journal publications.

Funding. This research received no external funding.

Competing interests. The author declares no competing interests. The affiliation with Precog Technologies is provided as a professional affiliation; Precog Technologies did not fund, sponsor or commission the work reported in this manuscript.

A Generator, inverse relations and limiting regimes

A.1 Characteristic exponent and cumulants

For one Cartesian component the marginal transfer density is

$$\mu_1(q) = \frac{r_d}{\sqrt{\pi}\hbar} \exp(-r_d^2 q^2/\hbar^2). \tag{47}$$

Its characteristic function is $\exp(-\sigma_q^2 s^2/2)$. Conditional on a Poisson event count N_T, the accumulated transfer is the sum of N_T independent draws. Averaging $\Phi_q(s)^{N_T}$ over N_T gives Eq. (8). The $2n$th derivative of this logarithm yields the *raw transfer moment* $\Gamma_D T \langle q^{2n} \rangle$, which is not the $2n$th cumulant of a single Gaussian kick. This distinction explains why a Gaussian transfer kernel can generate nonzero cumulants above order two in the finite-rate accumulated distribution.

Equation (9) gives

$$c_2 = \Gamma_D \sigma_q^2, \qquad c_4 = 3\Gamma_D \sigma_q^4, \tag{48}$$

$$c_6 = 15\Gamma_D \sigma_q^6, \qquad c_8 = 105\Gamma_D \sigma_q^8. \tag{49}$$

These four relations directly yield Eqs. (10), (12) and (13). Cumulant inversion requires finite moments and a resolved nonzero signal; it is not a regular estimation problem at $\Gamma_D = 0$. If the conventional background has independent increments, its cumulant production rates add. A preparation cumulant adds once per flight instead of growing with T, while terminal readout contributes its own distribution. Duration scans help separate those roles.

The position-space action of the generator is

$$\langle \mathbf{x}|\mathcal{L}_D \rho|\mathbf{x}'\rangle = -\Gamma_D \left[1 - \exp\left(-\frac{|\mathbf{x}-\mathbf{x}'|^2}{4r_d^2}\right)\right] \rho(\mathbf{x},\mathbf{x}'). \tag{50}$$

This follows by the Fourier transform of the normalized kernel. The equality between the characteristic exponent evaluated at $\mathbf{d}/\hbar$ and the decoherence rate is the established transfer–coherence correspondence [5]. The inversion and experimental comparison developed here use that correspondence rather than postulating a new independent visibility law.

For finite Γ_D and $r_d \to \infty$, transfers and decoherence at finite separation vanish. If Eq. (3) is imposed simultaneously at fixed M, R, $\Gamma_D \propto r_d^{-p}$ in this limit and the suppression is even stronger.

For $r_d \to 0$ at fixed positive Γ_D, the momentum-variance rate diverges while finite-separation decoherence approaches Γ_D. That ultraviolet limit requires a completion or cutoff and is not a controlled prediction of finite heating. Taking $\Gamma_D \to \infty$ and $r_d \to \infty$ with c_2 fixed instead gives the Brownian limit discussed in the text.

A.2 Mixture inequalities and their physical scope

For a positive rate measure on transfer variances, Cauchy–Schwarz gives

$$A_2^2 \le A_1 A_3, \qquad A_3^2 \le A_2 A_4. \tag{51}$$

Using $c_8 = 105A_4$ yields Eqs. (24) and (25). Equality requires a single nonzero variance up to sets of zero rate weight. Zero-amplitude events have no observable effect and their rate cannot be identified from the reduced dynamics.

The probability measure $w = u\nu/A_1$ weights channels by their contribution to the second cumulant. Consequently $\eta - 1$ measures the squared coefficient of variation of transfer variance under this weight. It is not directly the relative variance of physical aperture radii, because $u = \hbar^2/(2r^2)$ is nonlinear and the event-rate weighting matters. Interpreting it as a geometric distribution requires that extra inverse step and a microscopic model.

As a numerical check, rate weights $(0.7, 0.3)$ and dimensionless transfer variances $(0.4, 2)$ give $\eta = 1.24985$. The reproduction code verifies the lower and upper decoherence bounds for 500 logarithmically spaced separations. This is a consistency check on the analytic proof, not evidence that DJAMILAR apertures have such a distribution.

The inequalities concern a superposition of independent stationary channels, or its deterministic rate-measure limit. A rate drawn randomly once per run produces a mixture of complete run distributions and can add cumulants not described by A_j alone. Likewise, changing the initial-state distribution between runs is not an aperture mixture in this sense. These possibilities must be tested with time ordering and preparation records.

B Mechanical response and preparation

B.1 Free propagation and filtered observables

For a linear measured quantity Y, write the channel contribution as

$$Y_D = \sum_j h_T(s_j) q_j. \tag{52}$$

Poisson functional averaging gives

$$\ln \Phi_{Y_D}(k) = \Gamma_D \int_0^T \left[\exp\left(-\frac{k^2 \sigma_q^2 h_T(s)^2}{2} \right) - 1 \right] \mathrm{d}s. \tag{53}$$

Differentiation gives Eq. (16). If $H_n = \int h_T^n \mathrm{d}s$, then for an even-order response with $H_2, H_4 > 0$,

$$\sigma_q^2 = \frac{\kappa_4^{Y,D} H_2}{3\kappa_2^{Y,D} H_4}, \quad \Gamma_D = \frac{3(\kappa_2^{Y,D})^2 H_4}{\kappa_4^{Y,D} H_2^2}, \quad r_d^2 = \frac{3\hbar^2 \kappa_2^{Y,D} H_4}{2\kappa_4^{Y,D} H_2}. \tag{54}$$

For momentum, $h_T = 1$; for final free-flight position, $h_T = (T - s)/M$. A harmonic oscillator read out in position has $h_T(s) = \sin[\omega(T - s)]/(M\omega)$ in the ideal undamped case. Known damping and electronic filters modify this response and hence every H_n. Applying a force-noise calibration only to H_2 does not calibrate the fourth-cumulant response.

This order dependence is the time-domain counterpart of higher-order spectral filtering [20]. For a classical stochastic force with connected n-time correlation $C_n(t_1, \ldots, t_n)$, linear response gives

$$\kappa_n^Y = \int_0^T \cdots \int_0^T \left[\prod_{j=1}^{n} h_T(t_j) \right] C_n(t_1, \ldots, t_n)\, \mathrm{d}t_1 \cdots \mathrm{d}t_n.$$

The white compound-Poisson force has $C_n = c_n \delta(t_2 - t_1) \cdots \delta(t_n - t_1)$ and recovers Eq. (16). A colored environmental force requires its own multi-time correlations; matching its power spectrum alone does not determine its higher-order response. This extension specifies how to treat a background and does not replace the independent-increment channel assumed in the main derivation.

B.2 Initial quantum covariance

For free evolution before the terminal measurement,

$$X(T) = X(0) + \frac{T}{M} P(0) + X_D(T). \tag{55}$$

An initial Gaussian quantum state contributes the quadrature variance

$$B_{\mathrm{prep}} = V_X + \frac{T^2}{M^2} V_P + \frac{2T}{M} C_{XP}, \qquad V_X V_P - C_{XP}^2 \geq \frac{\hbar^2}{4}, \tag{56}$$

where $C_{XP} = \langle XP + PX \rangle / 2 - \langle X \rangle \langle P \rangle$. Its final quadrature marginal is Gaussian even when the initial state is pure. The stochastic channel is a convolution with that marginal for the homogeneous free dynamics. Independent Gaussian readout adds σ_{ro}^2; ordinary Gaussian momentum diffusion with variance-production rate D_{env} adds $D_{\mathrm{env}} T^3 / (3M^2)$.

Setting $C_{XP} = 0$ and minimizing over V_X at fixed uncertainty product gives Eq. (32). Negative covariance can focus a state at a chosen time [27], but the initial covariance, generating operations, trap-induced noise and readout backaction then belong in the model. No claim of a universal lower bound over all state preparations is made. Similarly, the assumed initial Gaussian must be verified: residual fourth and sixth preparation cumulants can bias the reconstruction even when its variance has been calibrated correctly.

B.3 Finite terminal readout duration

If the detector returns the mean position over $[T - \tau, T]$, with $0 < \tau \leq T$, its free-particle response to a kick at s is

$$h_{T,\tau}(s) = \begin{cases} (T - s - \tau/2)/M, & 0 \leq s \leq T - \tau, \\ (T - s)^2/(2M\tau), & T - \tau < s \leq T. \end{cases} \tag{57}$$

Hence, for the even n used in the inversions,

$$H_n = \frac{(T - \tau/2)^{n+1} - (\tau/2)^{n+1}}{M^n (n+1)} + \frac{\tau^{n+1}}{2^n M^n (2n+1)}. \tag{58}$$

The limit $\tau \to 0$ recovers $T^{n+1}/[(n+1)M^n]$. To first order, $H_n / H_n(0) = 1 - (n+1)\tau/(2T) + O[(\tau/T)^2]$. A terminal instantaneous-readout model is adequate only when this correction is negligible at the required precision, or when the exact response is applied. Finite windows also change the propagated initial-state quadrature and readout covariance. The synthetic example uses the instantaneous limit with additive readout error.

C Interference transfer and independent prediction

For the symmetric triangular path, $d(t) = 2d_{\max}t/T_I$ during the first half and $d(t) = 2d_{\max}(1 - t/T_I)$ during the second. Direct integration gives

$$\frac{1}{T_I}\int_0^{T_I} \exp[-d(t)^2/(4r_d^2)]\mathrm{d}t = \int_0^1 \exp[-d_{\max}^2 u^2/(4r_d^2)]\mathrm{d}u, \tag{59}$$

which yields Eq. (26). The path expression assumes that the selected interference contribution admits this separation history and that other dynamics are included in its conventional amplitude.

For a near-field experiment, let $A_j^{(0)}(M, v)$ denote the conventional complex amplitude of harmonic j, $w(M, v)$ the detected ensemble weight and $\Delta x_j(t; M, v)$ the relevant separation. The predicted amplitude takes the form

$$\overline{A}_j = \int \mathrm{d}M\mathrm{d}v\, w(M, v) A_j^{(0)}(M, v) \exp\{-\mathcal{D}[\Delta x_j(\cdot; M, v)]\}. \tag{60}$$

Normalization by the transmitted zeroth harmonic and any detector response must follow the actual signal definition. Averaging $\mathcal{D}$ before exponentiating is generally incorrect. Grating-induced incoherent processes also need their own propagation [22, 23, 28]. Equation (60) describes the required transfer structure; the numerical demonstration in this article uses a single selected mass and prescribed paths rather than the complete transfer matrix of a named apparatus.

For the synthetic coherence scan the probability of a "plus" output at a known phase extremum is

$$p_+(d_j) = \frac{1 + V_0 \exp[-\Gamma_D T_I K_\triangle(d_j, r_d)]}{2}, \qquad n_{+,j} \sim \text{Binomial}(N_j, p_+). \tag{61}$$

We use $V_0 = 0.8$, $N_j = 20\,000$, $T_I = T$ and $d_j = (12.5, 25, 40, 60, 90, 133, 200, 300)\,\text{nm}$. The inferred normalized contrast is $(2n_{+,j}/N_j - 1)/V_0$. Its standard error is $2\sqrt{p_+(1 - p_+)/N_j}/V_0$. In a real experiment, phase stability and uncertainty in V_0 must be estimated using control data rather than assumed.

The mechanical covariance in $(\ln\lambda, \ln a)$ is propagated through the forward model. Figure 3 uses 6 000 draws from the fitted asymptotic Gaussian parameter distribution. Its band is a pointwise parameter-prediction band, not a simultaneous confidence band or an interval including new counting noise. The residual statistic combines the count covariance with the correlated prediction covariance $J\Sigma_M J^\mathsf{T}$, where J is the derivative of the predicted contrast at the sampled separations. This accounts for the fact that the same mechanical calibration predicts all eight points. No parameters are fitted to those residuals, giving eight approximate degrees of freedom under the stated Gaussian linearization.

D Statistical precision, calibration and numerical validation

D.1 Cumulant covariance without a Gaussian sampling approximation

Let a centered symmetric measured variable have variance $v = S + B$, fourth cumulant k_4, sixth cumulant k_6 and eighth cumulant k_8. For N independent trials, the leading covariance of its second and fourth sample cumulants is

$$N\,\mathrm{Cov}\begin{pmatrix}\widehat{k}_2\\ \widehat{k}_4\end{pmatrix} = C = \begin{pmatrix}2v^2 + k_4 & 8vk_4 + k_6\\ 8vk_4 + k_6 & k_8 + 16vk_6 + 34k_4^2 + 72v^2k_4 + 24v^4\end{pmatrix}. \tag{62}$$

This result retains the non-Gaussian moments. It follows from the influence functions

$$\mathrm{IF}_2(x) = x^2 - v, \qquad \mathrm{IF}_4(x) = x^4 - 6vx^2 + 3v^2 - k_4. \tag{63}$$

For a symmetric distribution, estimating the mean does not add a first-order odd contribution to these influence functions. Finite-sample bias remains $O(1/N)$ for the moment estimators used in the supplied code and is assessed by the synthetic repetitions.

For a known Gaussian background, $\widehat{S} = \widehat{k}_2 - B$. At fixed mass, time and response, the logarithmic inverse has derivative matrix

$$G = \begin{pmatrix} (2S)^{-1} & -(2k_4)^{-1} \\ 2/S & -1/k_4 \end{pmatrix}, \qquad \mathrm{Cov}\begin{pmatrix} \ln \widehat{r} \\ \ln \widehat{\Gamma} \end{pmatrix} \simeq \frac{1}{N} G C G^{\mathsf{T}}. \tag{64}$$

The first row gives the requirements in Table 2. In momentum units σ_q, set $(S, k_4, k_6, k_8) = \lambda(1, 3, 15, 105)$. In position units $\sigma_q T/M$, use $S = \lambda/3$, $k_4 = 3\lambda/5$, $k_6 = 15\lambda/7$ and $k_8 = 105\lambda/9$. Both eighth moments are finite.

When $B \gg S$, the $24v^4$ term dominates. At fixed λ, the standard error scales as $N^{-1/2}\epsilon^{-2}$, so the required count grows as ϵ^{-4}. The Gaussian kurtosis error $\sqrt{24/N}$ would omit substantial higher-moment fluctuations when ϵ is near unity. The reference forecasts use the full covariance in Eq. (62).

An independently estimated background variance adds its uncertainty to that of S. If δB is a calibration bias, the moment inverse has first-order biases

$$\delta \ln r = -\frac{\delta B}{2S}, \qquad \delta \ln \Gamma = -\frac{2\delta B}{S}. \tag{65}$$

At $B = S$, a 1% error on B corresponds to a 0.5% radius bias and a 2% rate bias in this inverse. This is a useful scale for allocating calibration effort; the exact-density likelihood has its own nuisance-parameter correlations and should be profiled jointly. Similarly, position calibration scales, mass uncertainty and T uncertainty must be propagated through Eq. (15). In particular, a multiplicative displacement calibration error produces an opposite fractional shift of r at fixed M, T.

A concrete extension is to fit the dimensionless background variance jointly with the channel, using independent calibration observations z:

$$\mathcal{L}_{\mathrm{joint}}(\lambda, a, b) = \prod_{i=1}^{N} f(x_i \mid \lambda, a, b)\, \mathcal{L}_{\mathrm{cal}}(b; z).$$

For $\boldsymbol{\theta} = (\ln \lambda, \ln a)$ and a scalar nuisance b, the local information after profiling b is

$$F_{\mathrm{prof}} = F_{\theta\theta} - F_{\theta b}(F_{bb} + F_{bb}^{\mathrm{cal}})^{-1} F_{b\theta}.$$

Here F is the total information in the mechanical data and F_{bb}^{cal} is the independent calibration information. The known-background limit is $F_{bb}^{\mathrm{cal}} \to \infty$; finite calibration cannot improve that ideal precision. The control must characterize the same propagated background and its drift over the science runs. This nuisance-parameter extension has not been included in the numerical forecasts reported here.

D.2 Exact-density likelihood and computation

The density in Eq. (29) is obtained by a Fourier grid with 16 384 points over dimensionless $x \in [-40, 40)$. The Gaussian convolution makes the density smooth. The main likelihood evaluates the density by linear interpolation, clips only numerical tail values below 10^{-300} in the logarithm, and fits positive parameters in log coordinates. The fitted samples lie well within the grid. The numerical checks verify normalization and the second and fourth moments against their analytic values; a separate grid-convergence check accompanies the package.

Observed Hessians use symmetric finite differences with step 10^{-3} in log parameters. The design Fisher matrix is

$$I_{ij} = \int \frac{\partial_i f(x) \partial_j f(x)}{f(x)} \mathrm{d}x, \tag{66}$$

evaluated with parameter steps 10^{-4} and a probability cutoff $f > 10^{-12}$ for stable tail integration. Its inverse predicts the large-sample covariance of $(\ln \lambda, \ln a)$; $\ln r$ differs from $-\ln a$ only by a fixed unit offset. The likelihood forecasts in Figure 5 are shown only for $\epsilon \geq 0.08$, where the adopted grid resolves the broadened distribution. Moment formulas supply the smaller-fraction asymptote.

The mechanical synthetic generator independently samples a Poisson event count, uniform event times, Gaussian transfer amplitudes and Gaussian background. It does not generate samples from the discretized likelihood grid. The reference Monte Carlo uses 200 replicates of 30 000 trials and reports every replicate; no failed or negative moment result is silently discarded. In this reference calculation there are no negative moment reconstructions. Coverage is checked locally at the stipulated model and known background. It is not a goodness-of-fit test for an experimental channel.

D.3 Fixed-apparatus Fisher map

For the map in Section 6.6, use $a = (25\,\mathrm{nm})/r_d$ and $\lambda = \gamma_0 (M/m_0) F_4(R/r_d) T$ in Eq. (29). The apparatus and Gaussian convolution are fixed. Analytic differentiation gives

$$\partial_{\ln \lambda} \Phi_x(k) = \Phi_x(k) \lambda [J(ak) - 1], \tag{67}$$

$$\partial_{\ln a} \Phi_x(k) = \Phi_x(k) \lambda [\mathrm{e}^{-(ak)^2/2} - J(ak)], \tag{68}$$

because $zJ'(z) = \mathrm{e}^{-z^2/2} - J(z)$. Fourier inversion of these expressions gives the two density derivatives used in I_{ij}. Both parameters are estimated jointly; using only $I^{-1}_{\ln a, \ln a}$ would incorrectly treat the event rate as known. The transformation to $(\ln \gamma_0, \ln r_d)$ is invertible for positive rate and size, so this profiling also allows the normalization to vary freely despite its aperture-dependent activation.

The map evaluates 82 radii between 8 and 100 nm and 111 normalizations between 5×10^{-10} and $5 \times 10^{-3}\,\mathrm{s}^{-1}$, retaining points between the two declared boundaries. Its Fourier grid contains 16 384 points over $[-80, 80)$ with cutoff $f > 10^{-12}$. Contour rates are solved by root finding rather than read from pixels. At the reference point and at five points on the 30% contour, doubling the window and grid changes s_r by less than 10^{-9} relatively. Raising the density cutoff to 10^{-10} changes it by less than 8×10^{-5} relatively. The reference result agrees with the independent finite-difference score calculation in the original simulation.

The map does not perform maximum-likelihood fits or import the reference optimizer's search bounds. In particular, the original fit range $0.03 \leq \lambda \leq 30$ is a numerical setting for its reference samples, not a physical lower limit. The 30% contour at 25 nm has $\lambda = 0.02310$. Any finite-sample coverage study there must expand the fitting range and treat the weak-rate boundary explicitly. The map provides an asymptotic design calculation; background calibration uncertainty and coverage away from the reference point remain to be evaluated.

D.4 Activation likelihood and limited experimental scope

For the activation illustration, physical radii are $(10, 13, 17, 21, 25, 30, 38, 48)$ nm. Masses follow the fixed density $971\,\mathrm{kg\,m}^{-3}$. Exposure T_i is the inverse rate of the reference model at that size, fixed before generating either scenario. The count probability is

$$p_{+,i} = \frac{1 + V_0 \exp\{-\Gamma(M_i, R_i; r_A, \gamma_0) T_i [1 - \mathrm{e}^{-300^2/(4 \cdot 25^2)}]\}}{2}. \tag{69}$$

Lengths in the last exponential are in nanometres. Each size uses 20 000 trials. Only $\ln \gamma_0$ and $\ln r_A$ are fitted. The incompatible scenario changes the generating r_A to 35 nm while keeping all prescribed exposures and the resolving width fixed. It therefore supplies a test of a failed common-length identification rather than a redefined exposure schedule that conceals the discrepancy.

This synthetic scan assumes preparation of the stipulated paths, a known harmonic contrast, exact size calibration and adequate detection. Its likelihood does not include the engineering operations that produce a separated state on a microsecond time scale. Those are required for a physical realization and are explicitly distinct from the statistical-identification result.

E Sphere form factors and the CSL diagnostic

For an isotropic transfer measure, the angular average of the $2n$th power of one direction cosine is $1/(2n+1)$. Combining this with the three-dimensional radial measure $q^2 \mathrm{d}q$ gives Eq. (41). Treating $F(qR/\hbar)^2$ as a one-dimensional transfer distribution would miss both this factor and the radial power, and would give different diagnostics.

In the point-body limit, $F \to 1$ and

$$J_n(0) = \frac{\Gamma(n+3/2)}{2(2n+1)}, \tag{70}$$

where Γ is the Euler gamma function. Thus both effective radii tend to r_C and $c_6 c_2 / c_4^2 \to 5/3$, as required for the Gaussian generator. The normalization also becomes the standard point-mass CSL rate $\lambda_{\mathrm{CSL}}(M/m_0)^2$, in the usual convention where λ_{CSL} is the reference-mass localization rate [8]. This quadratic amplification differs from the reference DJAMILAR choice even when the transfer shapes coincide.

Expanding the form factor gives

$$F(z)^2 = 1 - \frac{z^2}{5} + \frac{3z^4}{175} + O(z^6), \tag{71}$$

$$\frac{J_n(\xi)}{J_n(0)} = 1 - \frac{n+3/2}{5}\xi^2 + \frac{3(n+3/2)(n+5/2)}{175}\xi^4 + O(\xi^6). \tag{72}$$

Series division and square rooting then yield

$$\frac{r_{M,24}}{r_C} = 1 + \frac{\xi^2}{10} + \frac{\xi^4}{200} + O(\xi^6), \tag{73}$$

$$\frac{r_{M,46}}{r_C} = 1 + \frac{\xi^2}{10} + \frac{11\xi^4}{1400} + O(\xi^6). \tag{74}$$

Their squared ratio gives Eq. (43). The leading shift of each effective radius is quadratic in size, while their relative discrepancy begins at fourth order. This explains why the mixture-bound violation is much smaller than the common shift near the point limit.

For $\xi \to \infty$, the leading oscillatory form-factor contribution is $9\cos^2(\xi k)/(\xi^4 k^4)$. The region $k = O(\xi^{-1})$ contributes $O(\xi^{-2n-3})$, subleading for $n \geq 1$. Averaging the remaining rapid oscillations gives

$$J_n(\xi) \sim \frac{9}{2(2n+1)\xi^4} \int_0^\infty k^{2n-2} \mathrm{e}^{-k^2} \mathrm{d}k = \frac{9\Gamma(n-1/2)}{4(2n+1)\xi^4}, \quad n \geq 1. \tag{75}$$

Consequently $J_1/J_2 \to 10/3$, $J_2/J_3 \to 14/15$ and $J_3 J_1 / J_2^2 \to 25/7$, proving Eq. (44). This asymptote uses a homogeneous sphere with a sharp boundary and Gaussian CSL smearing; changing its surface profile requires repeating the calculation.

The supplied code evaluates the integrals with $F(z) = 3j_1(z)/z$, where j_1 is the spherical Bessel function, and adaptive quadrature over $0 \leq k \leq 14$. The Gaussian factor makes the omitted tail negligible. Multiplying the integrand by $\max(1, \xi^4)$ before integration controls absolute-tolerance errors at large size. Numerical checks recover the small-size series, the minimum and return crossing, and the large-size limits to better than 10^{-3} relatively at $\xi = 100$. These are checks of theoretical population ratios, not a simulation of their measurement errors.

F Provenance, result status and reproducibility

The notation A–D below separates a direct consequence (A), a new deduction solidly motivated within the stated model (B), a research hypothesis requiring additional physical input (C), and distant speculation (D). It assesses logical status, not empirical confirmation or priority across the literature. No D-level claim is used in this paper.

Table 5: Origin and logical status of the principal developments.

Development	Trigger and reasoning	Status
Mechanical aperture inverse	Exact generator and Wigner transfer in Ref. [3], Sections 3–6; retain finite-event cumulants before diffusion.	A, conditional on the generator.
Mechanical prediction of coherence	Ref. [3]'s coherence–noise link and resolving scan; combine with the new inverse and an independent path response. General correspondence: Ref. [5].	B as an operational cross-test.
Gaussian-mixture bound and ordered radii	Positive Gaussian kernel in Refs. [2, 3]; extend by a positive rate measure and apply convexity and moment inequalities.	B for the theorem; C for geometric heterogeneity.
Preparation ratio and mass cancellation	Collective activation in Ref. [3]; exact free-flight response and Gaussian quantum uncertainty.	B within the stated preparation class.
Common aperture in experiment	Two length reconstructions in Ref. [3], Section 8, plus the mechanical route and independent calibration.	C for physical realization; simulations are conditional.
CSL sphere diagnostic	Apply the mechanical inverses to the standard rigid-body form factor [19]; evaluate ratios and asymptotes.	A for the formulas; B for the comparative test.
Fixed-apparatus sensitivity map	Exact measured-density likelihood, activation law and unchanged preparation budget.	B as a conditional forecast; coverage remains local.
Gravitational-state reconstruction	Loading and state in Ref. [2], Sections 2 and 5; use independently reconstructed radius ratios.	A for the algebra; C for a predicted local state transfer.

The package contains editable LaTeX, seven figures, all synthetic samples, count tables, results and forecasts. Figures are vector graphics except the map's rasterized colour field. The reproduction directory contains `reproduce.py`, `validate.py` and `extensions.py`; the README lists commands. `results.json` records the original simulation, while `extensions_results.json` records CSL diagnostics, thresholds and convergence checks. Original samples and Monte Carlo outputs are unchanged.

Seeds are fixed as 240924 (mechanics), 240925 (coherence), 240926 (common activation), 240927 (shifted activation), 240928 (prediction band) and 240929 (Monte Carlo). The reference execution uses Python 3.12.14, NumPy 2.3.5, SciPy 1.17.0 and Matplotlib 3.10.8. SI constants are taken from SciPy; results are evaluated with dimensionless distributions and stable cumulant ratios to avoid underflow from high powers of SI momentum. The chosen 25 nm unit in the numerical fit does not constrain the reconstructed radius.

References

[1] A. Zerouta, *Gravity as Geometric Filtration: A Unified Framework for Cosmological and Quantum Phenomena*, Research Square preprint (2025). doi:10.21203/rs.3.rs-6570489/v1.

[2] A. Zerouta, *DJAMILAR: Gravity as Geometric Filtration—A Common Geometric Origin of Gravitation, Quantum-Classical Behaviour and Dark-Sector Phenomenology*, Research Square preprint, version 1 (2026). doi:10.21203/rs.3.rs-11144964/v1.

[3] A. Zerouta, *Djamilar-Induced Localization and the Quantum-Classical Transition*, Research Square preprint, version 1 (2026). doi:10.21203/rs.3.rs-11162349/v1.

[4] A. S. Holevo, "On translation-covariant quantum Markov equations," *Izvestiya: Mathematics* **59**, 427–443 (1995). doi:10.1070/IM1995v059n02ABEH000019.

[5] B. Vacchini, "Theory of Decoherence due to Scattering Events and Lévy Processes," *Physical Review Letters* **95**, 230402 (2005). doi:10.1103/PhysRevLett.95.230402. arXiv:quant-ph/0510127.

[6] B. Vacchini and K. Hornberger, "Quantum linear Boltzmann equation," *Physics Reports* **478**, 71–120 (2009). doi:10.1016/j.physrep.2009.06.001.

[7] G. C. Ghirardi, A. Rimini and T. Weber, "Unified dynamics for microscopic and macroscopic systems," *Physical Review D* **34**, 470–491 (1986). doi:10.1103/PhysRevD.34.470.

[8] A. Bassi, K. Lochan, S. Satin, T. P. Singh and H. Ulbricht, "Models of wave-function collapse, underlying theories, and experimental tests," *Reviews of Modern Physics* **85**, 471–527 (2013). doi:10.1103/RevModPhys.85.471.

[9] B. Buchmann and R. Grübel, "Decompounding: An estimation problem for Poisson random sums," *The Annals of Statistics* **31**, 1054–1074 (2003). doi:10.1214/aos/1059655905.

[10] L. M. Norris, G. A. Paz-Silva and L. Viola, "Qubit Noise Spectroscopy for Non-Gaussian Dephasing Environments," *Physical Review Letters* **116**, 150503 (2016). doi:10.1103/PhysRevLett.116.150503.

[11] Y. Sung, F. Beaudoin, L. M. Norris et al., "Non-Gaussian noise spectroscopy with a superconducting qubit sensor," *Nature Communications* **10**, 3715 (2019). doi:10.1038/s41467-019-11699-4.

[12] K. Hornberger, S. Uttenthaler, B. Brezger, L. Hackermüller, M. Arndt and A. Zeilinger, "Collisional decoherence observed in matter wave interferometry," *Physical Review Letters* **90**, 160401 (2003). doi:10.1103/PhysRevLett.90.160401.

[13] L. Hackermüller, K. Hornberger, B. Brezger, A. Zeilinger and M. Arndt, "Decoherence of matter waves by thermal emission of radiation," *Nature* **427**, 711–714 (2004). doi:10.1038/nature02276.

[14] Y. Y. Fein, P. Geyer, P. Zwick et al., "Quantum superposition of molecules beyond 25 kDa," *Nature Physics* **15**, 1242–1245 (2019). doi:10.1038/s41567-019-0663-9.

[15] S. Pedalino, B. E. Ramírez-Galindo, R. Ferstl, K. Hornberger, M. Arndt and S. Gerlich, "Probing quantum mechanics with nanoparticle matter-wave interferometry," *Nature* **649**, 866–870 (2026). doi:10.1038/s41586-025-09917-9.

[16] A. Vinante, R. Mezzena, P. Falferi, M. Carlesso and A. Bassi, "Improved Noninterferometric Test of Collapse Models Using Ultracold Cantilevers," *Physical Review Letters* **119**, 110401 (2017). doi:10.1103/PhysRevLett.119.110401.

[17] A. Vinante, M. Carlesso, A. Bassi et al., "Narrowing the Parameter Space of Collapse Models with Ultracold Layered Force Sensors," *Physical Review Letters* **125**, 100404 (2020). doi:10.1103/PhysRevLett.125.100404.

[18] M. Carlesso, S. Donadi, L. Ferialdi, M. Paternostro, H. Ulbricht and A. Bassi, "Present status and future challenges of non-interferometric tests of collapse models," *Nature Physics* **18**, 243–250 (2022). doi:10.1038/s41567-021-01489-5.

[19] L. Ferialdi and A. Bassi, "CSL reduction rate for rigid bodies," *Physical Review A* **102**, 042213 (2020). doi:10.1103/PhysRevA.102.042213.

[20] D. R. Brillinger, "An Introduction to Polyspectra," *The Annals of Mathematical Statistics* **36**, 1351–1374 (1965). doi:10.1214/aoms/1177699896.

[21] N. Piccione, "Diffusion Minimization via Optimal Smearing in Collapse and Hybrid Classical-Quantum Gravitational Models," *Physical Review A* **113**, 062211 (2026). doi:10.1103/h74z-zvfv. arXiv:2511.00644.

[22] K. Hornberger, J. E. Sipe and M. Arndt, "Theory of decoherence in a matter wave Talbot–Lau interferometer," *Physical Review A* **70**, 053608 (2004). doi:10.1103/PhysRevA.70.053608.

[23] S. Nimmrichter, K. Hornberger, P. Haslinger and M. Arndt, "Testing spontaneous localization theories with matter-wave interferometry," *Physical Review A* **83**, 043621 (2011). doi:10.1103/PhysRevA.83.043621.

[24] M. Armano, H. Audley, J. Baird et al., "Beyond the Required LISA Free-Fall Performance: New LISA Pathfinder Results down to 20 microhertz," *Physical Review Letters* **120**, 061101 (2018), with the publisher's abstract correction of 21 February 2018. doi:10.1103/PhysRevLett.120.061101.

[25] J. Millen, T. S. Monteiro, R. Pettit and A. N. Vamivakas, "Optomechanics with levitated particles," *Reports on Progress in Physics* **83**, 026401 (2020). doi:10.1088/1361-6633/ab6100.

[26] U. Delić, M. Reisenbauer, K. Dare, D. Grass, V. Vuletić, N. Kiesel and M. Aspelmeyer, "Cooling of a levitated nanoparticle to the motional quantum ground state," *Science* **367**, 892–895 (2020). doi:10.1126/science.aba3993. Preprint: arXiv:1911.04406.

[27] H. P. Yuen, "Contractive States and the Standard Quantum Limit for Monitoring Free-Mass Positions," *Physical Review Letters* **51**, 719–722 (1983). doi:10.1103/PhysRevLett.51.719. Erratum: **51**, 1603 (1983), doi:10.1103/PhysRevLett.51.1603.3.

[28] M. Toroš and A. Bassi, "Bounds on quantum collapse models from matter-wave interferometry: calculational details," *Journal of Physics A: Mathematical and Theoretical* **51**, 115302 (2018). doi:10.1088/1751-8121/aaabc6.

[29] S. Nimmrichter, K. Hornberger and K. Hammerer, "Optomechanical sensing of spontaneous wave-function collapse," *Physical Review Letters* **113**, 020405 (2014). doi:10.1103/PhysRevLett.113.020405.

[30] A. Tilloy, "Ghirardi-Rimini-Weber model with massive flashes," *Physical Review D* **97**, 021502 (2018). doi:10.1103/PhysRevD.97.021502.

[31] N. Piccione, "Gravitational Poissonian Spontaneous Localization Model of Hybrid Quantum-Classical Newtonian Gravity: Energy Increase and Experimental Bounds," *Classical and Quantum Gravity* **43**, 165005 (2026). doi:10.1088/1361-6382/ae92e5. arXiv:2602.19377.

[32] J. Oppenheim, C. Sparaciari, B. Šoda and Z. Weller-Davies, "Gravitationally induced decoherence vs space-time diffusion: testing the quantum nature of gravity," *Nature Communications* **14**, 7910 (2023). doi:10.1038/s41467-023-43348-2.